

NUMERICAL MODELING OF BRIDGMAN GROWTH OF PbSnTe IN A MAGNETIC FIELD

Minwu Yao

Ohio Aerospace Institute, Brook Park, OH 44142

Arnon Chait

NASA Lewis Research Center, Cleveland, OH 44135

Archibald L. Fripp and William J. Debnam

NASA Langley Research Center, Hampton, VA 23665

ABSTRACT

In this work we study heat and mass transport, fluid motion and solid/liquid phase change in the process of steady Bridgman growth of $\text{Pb}_{0.8}\text{Sn}_{0.2}\text{Te}$ (LTT) in an axially-imposed uniform magnetic field under terrestrial and microgravity conditions. In particular, this research is concerned with the interrelationships among segregation, buoyancy-driven convection and magnetic damping in the LTT melt. The main objectives are to provide a quantitative understanding of the complex transport phenomena during solidification of the non-dilute binary of LTT, to provide estimates of the strength of magnetic field required to achieve the desired diffusion-dominated growth, and to assess the role of magnetic damping for space and earth based control of the buoyancy-induced convection. The problem was solved by using FIDAP[†] and numerical results for both vertical and horizontal growth configurations with respect to the acceleration of gravity vector are presented.

[†] NASA does not endorse commercial products. Details about the products named in this paper were included for completeness and accuracy. No endorsement or criticism of these products by NASA should be assumed.

1. INTRODUCTION

Direct, quantitative analysis of convection and solute segregation in molten metals and semiconductors is particularly difficult. These materials are generally opaque, which hinders non-intrusive measurements. Thus, most studies are limited to indirect measurement techniques. The role of numerical modeling then becomes crucial in analyzing the system. A better understanding of the complex relationship among thermal conditions, natural convection, growth morphology, and macrosegregation in solidification process can be achieved through synergistic theoretical [1,2] and numerical analysis [3,4] in combination with various experiments on earth and in space. In numerical modeling, the geometry, furnace temperature settings, materials and other parameters can be easily altered and the impact of the changes in design parameters can then be examined in a more efficient and economic way. The full-scale modeling combined with the scaling and asymptotic analysis provides a convenient and useful tool for the furnace design and growth condition optimization.

Directional solidification, such as Bridgman growth, has been widely used in space experiments and in many industrial processes for electronic materials. As one of the most fundamental arrangements, Bridgman growth is of significant technological importance, both from experimental and numerical points of view. Therefore, in this paper we shall focus on the modeling of Bridgman growth. However, once validated, the model and numerical techniques developed in this work are generally applicable to a number of solidification processes.

During crystal growth, temperature and concentration gradients often induce natural convection. It has been shown both experimentally and numerically that the flow mode, the shape of the solid/liquid interface and the thermal and solute profiles in a solidifying liquid are greatly affected by natural convection. The variation of convective strength has a direct impact on solute distribution (segregation). The distortion of the interface, in turn, affects convection. Thus a complex interaction exists among convection, thermal and solutal gradients and interface shape.

In the vertical Bridgman growth, the furnace is assumed to be aligned perfectly parallel to gravity vector. This arrangement results in a great simplification for numerical treatment. In this case, the flow, thermal and solutal fields may be taken to be axi-symmetric, which is valid for laminar flow and axi-symmetric boundary conditions. When convection gains enough strength, the flow on the axi-symmetric plane forms one or multiple torus-like

cells [5], depending on the local thermal and solutal gradients. At 1-g level, the magnitude of the convective flow may be very high, resulting in time-dependent or even turbulent flows requiring transient 3-D analysis [6,7].

Another fundamental Bridgman arrangement is the horizontal configuration in which the furnace axis is aligned perpendicular to the gravity vector. As shown by Arnold et al [8], the flow mode during 1-g horizontal growth is the so-called *shallow cavity flow* with a complex 3-D structure. During shuttle flight in space, however, the magnitude and orientation of the gravity vector are generally a priori unknown functions of time (unsteady). Consequently, the flow structure and segregation fields in the solidifying liquid during space growth are still theoretically unknown.

In the solidification process, solute concentration at the interface is affected by the removal rate of excess solute rejected at the moving interface. Under ideal conditions (no convection), the rejected solute is transported by diffusion only. In reality, however, the transport of excess solute to and from the interface is greatly affected by additional factors such as the natural convection. In this study we consider buoyancy forces induced by both thermal expansion and compositional differences. For PbSnTe, it is important to note that the magnitude of density variations due to thermal and solute gradients are globally of the same order and a positive change of ΔT and ΔC will reduce the density in the buoyancy term in the momentum equation. The segregation coefficient $k < 1$ and $\rho_{\text{solute}} < \rho_{\text{solvent}}$ imply that lighter solute is rejected at the interface. Consequently, the double-diffusive convection is solutally unstable in a classical vertical growth system.

The conventional segregation quantity provided by experimental measurement is the effective segregation coefficient defined as the ratio of the concentration in the crystal to that in the bulk of the melt. Due to the existence of a solute boundary layer adjacent to the solid/liquid interface during the solidification process, this quantity differs from the interface segregation coefficient, which is calculated by the ratio of solute concentration in the grown crystal to that at the liquid side of the interface. The difference between these two quantities will depend on the structure and strength of the flow in the melt as well as on the growth rate. When flow is dominated by natural convection, the relationship between these quantities and the complex interactions among the driving forces can be obtained only from a full numerical simulation [9].

The idea of using a magnetic field to damp melt turbulence and thereby improve microscopic homogeneity of the crystal was introduced in 1966 independently by Utech and

Flemings [10,11] and by Chedzey and Hurle [12]. It was shown in their work that a transverse magnetic field damped temperature fluctuations in the horizontal directional solidification of tin and InSb. In 1981 workers at Sony in Japan [13] developed a growth process using a static transverse magnetic field generated by an external electromagnet. Since then there has been considerable amount of research efforts pertaining to the magnetic damping in the growth of silicon, the III-V compound semiconductor, gallium arsenide, and indium phosphide, etc. [14]. Motivation for the use of an applied magnetic field has been widened subsequently. In addition to damping out the chaotic and time-periodic convection in the melt and consequently reducing fluctuations in solute concentration, magnetic field can also be used to control the growth conditions at various stages in the growth process. For instance, the alteration of the laterally averaged axial concentration of oxygen is one of the primary advantages of using magnetic damping in Czochralski growth of silicon [15,16].

There are several different configurations of the applied magnetic field reported in the literature. The axial and transverse fields are perhaps the simplest configurations among them. In addition, the concept of a configured field [17,18] was also developed to tailor the field configuration to the flows in the melt so that only the harmful flows are damped while the beneficial flow patterns are still retained. One such configured field is the cusped field formed with a pair of Helmholtz coils operated in opposed-current mode. The most extensive work to date, however, has been on the axial magnetic field.

The application of steady-state magnetic fields offers a practical means of suppressing natural convection due to both the steady and unsteady changes in the residual acceleration. When an axial magnetic field is imposed, its effect on the convection in the melt is to interfere with the radial velocity component. As shown by asymptotic analysis [46,19], the magnitude of the radial velocity decreases proportionally to the square of B , the strength of the magnetic field. When B is sufficiently intense, an almost uniaxial flow, and hence the desired diffusion-dominant growth condition, may be obtained.

In the literature, previous studies on vertical Bridgman growth with magnetic damping include both experimental and numerical efforts. K.M. Kim [20] grew InSb with a magnetic field greater than 1.7 Kilo-Gauss (KG) and obtained a striation free boule. The most obvious effect of an increasing magnetic field was the reduction and then the elimination of temperature fluctuations in the melt. Sen et al [21] found that a 2 KG transverse magnetic field was sufficient to statistically reduce the number of area defects in InGaSb, but was insufficient to produce an observable effect on the composition distribution. Matthiesen

et al. [22] demonstrated melt stabilization in doped germanium when grown in a 30 KG axial magnetic field. They observed a transition from convection dominated to diffusion controlled growth, for the dopant atoms, via the application of the magnetic field. Su, Lehoczky and Szofran [23] grew HgCdTe and HgZnTe in a 5 KG transverse field. Their results show a strong coupling between convection and the magnetic field but they were unable to fully suppress convection.

In the pioneering numerical magnetic interaction studies for vertical Bridgman growth [19], D.H. Kim et al performed a finite element analysis for the growth of dilute Ga doped Ge. Their study shows that the compositional radial non-uniformity is greatest for an intermediate field strength. Stronger fields suppress convective flow completely and lead to uniform solute segregation across the crystal and to diffusion-controlled axial segregation. They calculated that the effect of the magnetic field was very similar to reducing gravity for vertical growth. Motakef [24] has analyzed the growth of Ge, GaAs and CdTe in both low gravity and magnetic fields. He computed the ranges of ampoule sizes and gravity level or field strength where these single component materials could be grown under diffusion control. In a more recent work, Prescott and Incropera [25] simulated magnetically damped convection in solidifying Pb₁₉Sn alloy. Their results show that magnetic damping significantly affects thermally driven flows during early stage of solidification. However, interdendritic flows and macrosegregation patterns are not significantly altered by moderate magnetic fields. Their scaling analysis suggests that extremely strong fields would be required at 1-*g* to effectively dampen convection patterns that contribute to macrosegregation. Simulations in their work were based on a continuum model for dendritic solidification systems [26]. In [27], their work was extended to account for turbulent flow and to application of a time varying magnetic field which augments thermal buoyancy forces in the melt while opposing solutal buoyancy forces in the mushy zone. Due to the complexity of the problem and the large number of parameters involved, it is difficult to obtain the whole picture of the physical phenomena from numerical simulation alone. Hjellming and Walker [47-49] have therefore used asymptotic analysis to deduce the nature of the boundary layers formed.

Among the previous efforts cited above, only two studies [21,23] involve the melt stabilization of a non-dilute multicomponent system. One important consideration for analysis of non-dilute alloys is the need to include the density variation due to compositional differences. For non-dilute alloys, our results (and the results in [5]) show that the effect of

the compositional derived density differences is important and should not be neglected. Furthermore, the non-trivial interaction between the thermal and the solutal fields and their coupled effects on the flow field in the melt through the buoyancy force term intricately depend on the magnitude and orientation of the gravity vector. Therefore we cannot decipher the interactive thermal and solutal effects *a priori* by order-of-magnitude analysis of the non-dimensional groups alone.

In this study, we extend previous works in this area to non-dilute multicomponent systems and to the combined effect of magneto-hydrodynamic (MHD) and low gravity stabilization. In particular, this research is concerned with the study of the effects of an axial magnetic field on the Bridgman growth of $\text{Pb}_{0.8}\text{Sn}_{0.2}\text{Te}$ with convective flows induced by both thermal and solutal buoyancy forces. To this purpose, a complete 2-D (including axi-symmetric) finite element model (for full-coupled flow, thermal and solutal fields) has been established. The model considers the coupled momentum, energy, and mass transport equations with the Boussinesq approximation applied to the temperature and concentration buoyancy terms. The influence of the magnetic field on the flow is expressed through the Lorentz force. The temperature of the solid-melt interface is determined from the phase diagram. The interface position is simultaneously solved using the front tracking approach in conjunction with a deformable mesh. The furnace temperature profile is imposed through a heat transfer boundary condition on the outer surface of the cartridge, details of which were determined from previous experimental data. The so-called pseudo-steady-state-model [5,19] is used to simulate the steady growth in both axial and horizontal Bridgman configurations. The problem is solved by the commercial code FIDAP [28].

The primary objectives of this study are to provide a quantitative understanding of the complex transport phenomena during solidification of non-dilute binarys, to furnish a numerical tool for furnace design and growth condition optimization, to provide estimates of the required magnetic field strength for low gravity growth, and to assess the role of magnetic damping for space and earth control of the double-diffusive convection. These objectives will be achieved via a systematic examination of the heat and mass transport and fluid flow phenomena using both earth and reduced gravity conditions, and by using MHD damping at various gravity levels. As an integral part of a NASA research program, our numerical simulation collaborates and supports both the flight and ground-based experiments in an effort to bring together a complete picture of the complex physical phenomena involved in the crystal growth process.

In order to provide a solid theoretical foundation for this work, this paper will be devoted to the modeling studies, leaving a more detailed description of the experimental work for subsequent reports.

2. EXPERIMENTAL BACKGROUND

The experiment [29,30] modeled in this paper studies the effect of the gravitational body force on the convective properties of the alloy compound semiconductor, PbSnTe (LTT), with body forces modified by both reduced gravity and by MHD. PbSnTe is an ideal material for this study because it was used in both a past flight experiment and a planned AADSF (Automated Advanced Directional Solidification Furnace) experiment. Both of these experiments are without magnetic field. Subsequent experiments using MHD, including earth based and in space, will form a comprehensive set of space processing experiments which will help to elucidate the gravity dependent physical phenomena for the growth of this class of materials.

The bulk growth of this material is interesting from a purely scientific point of view, because the liquid is always solutally or thermally unstable. For the vertical growth, one of the pertinent fields, either temperature or concentration, will be in a stable orientation and the other field will be in an unstable orientation. This double convective instability cannot be made stable by simply balancing thermal and solutal expansion with a high temperature gradient [31].

PbSnTe is a semiconductor material with a compositional dependent energy bandgap which is adjustable from 0 eV ($\approx 40\%$ SnTe) to 6.4 eV ($\approx 100\%$ PbTe). It is a direct bandgap material hence it can be used for both infrared lasers and detectors. The utilization of this and other materials in this general class is dependent on both the crystalline perfection of the material and the compositional homogeneity.

The first flight experiment, without magnetic field, in this series was on STS 61A in October 1985 [32]. It was shown that a high degree of convection was still apparent at the low growth rates used. The convective instability may have been exacerbated because the crystal axis and the steady state residual acceleration vectors were (estimated) perpendicular. The analysis of this flight sample served as a basis of continued ground based research and the development of the existing flight experiment. Previous studies show that the growth of PbSnTe is totally dominated by gravity driven convection on earth and is still strongly influenced by convection in space growth. These two facts make PbSnTe an ideal material for studying the effects of MHD damping on earth and in space.

The experiment consists of two parallel programs, the ground-based growth in the superconductor magnetic furnace and the space growth in a magnetically damped furnace. The ground-based experiments are conducted at MSFC where a crystal growth furnace with a 50 KG axial magnet and another furnace with a 5 KG transverse magnet have been developed. After growth, the samples are evaluated for compositional uniformity and defect structure. The compositional profile is the most sensitive measure of convection intensity during growth and is measured by a wavelength dispersive electron micro-probe. The planned flight experiment has basically the same design as that of the AADSF experiment but with the addition of the stabilizing magnetic field.

The typical experimental parameters, such as the ampoule dimensions, temperature gradient, etc., are listed in Table 1. The ampoule materials are quartz and InconelTM. The thermophysical properties of PbSnTe can be found in refs. [29,33-36]. The phase Diagram is given in [37]. The electrical conductivity can be found in [38]. Other material properties are given in [39]. A typical thermal profile measured along the center of the ampoule is shown in Fig. 1. This profile is used as the reference temperature in the heat transfer boundary condition imposed in the modeling.

3. THEORETICAL BACKGROUND

3.1 Governing Equations

In this paper, we consider heat and mass transport, fluid motion and solid/liquid phase changes in the crystal growth process. In particular, the liquid pseudo-binary mixture of LTT is assumed to behave as a Newtonian fluid and its motion is described by the following Navier-Stokes equation:

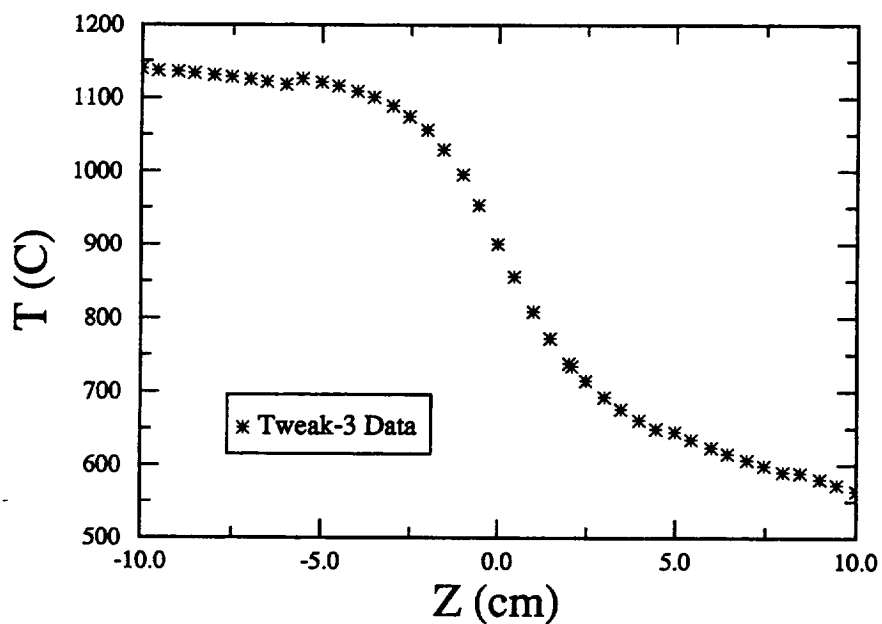
$$\rho_0 \left(\frac{\partial \mathbf{u}}{\partial t} + \mathbf{u} \cdot \nabla \mathbf{u} \right) = - \nabla p + \nabla \cdot \{ \mu(T) [\nabla \mathbf{u} + (\nabla \mathbf{u})^T] \} \quad (1a)$$

$$+ \rho_0 \mathbf{g} [1 - \beta_t(T - T_0) - \beta_c(C - C_0)] + \sigma_m (\mathbf{u} \times \mathbf{B}) \times \mathbf{B}$$

where \mathbf{u} is the velocity vector, ρ_0 is fluid density at the reference temperature T_0 , p is pressure, μ is viscosity, T is the temperature variable, \mathbf{g} is the acceleration of gravity, β_t and β_c are thermal and solutal volumetric expansion coefficients. The Boussinesq model is adopted to approximate the buoyancy force caused by density variation with both temperature and concentration. A uniform magnetic field, \mathbf{B} , is imposed in the axial direction of the furnace. When the ampoule and crystal are moved parallel to \mathbf{B} , the imposed magnetic field does not cause a current in the materials. The electric field is everywhere equal to

Table 1. Experimental Design Parameters for the Vertical Bridgman Growth

Parameter	Symbol	Value
Ampoule Length	L	11 cm
Sample Radius	R	0.5 cm
Ampoule Outer Radius	R_a	0.7 cm
Thermal Gradient	dT/dz	$\approx 80^\circ\text{C}/\text{cm}$
Growth Velocity	V_g	1cm/hour
Hot Zone Temperature	T_h	1150°C
Cold Zone Temperature	T_c	550°C
Temperature Difference	$\Delta T = T_h - T_c$	600K

**Figure 1.** Temperature profile obtained using a quartz sample (Ca19). It was measured along the sample centerline with the furnace set to 525/575/1150/1150/1150 and the sample translated at a speed of 2 cm/hour.

zero and the magnetic induction is not distorted by convection in the melt. Therefore the only effect of the magnetic field is the Lorentz body force term in eqn. (1), where σ_m is the electrical conductivity of the melt.

The LTT liquid is assumed to be incompressible and the incompressibility condition is given by

$$\nabla \cdot \mathbf{u} = 0 . \quad (2)$$

The heat transport is controlled by the balance of thermal energy

$$\rho_0 c_p \left(\frac{\partial T}{\partial t} + \mathbf{u} \cdot \nabla T \right) = \nabla \cdot [\kappa(T) \nabla T] \quad (3a)$$

where c_p is specific heat and κ is thermal conductivity. The solute transport is governed by the balance of species concentration

$$\frac{\partial C}{\partial t} + \mathbf{u} \cdot \nabla C = \nabla \cdot (D \nabla C) \quad (4a)$$

where C is the concentration of impurity and D denotes the mass diffusion coefficient. On each segment of the boundary, it is necessary to prescribe appropriate boundary conditions. Details of the computational boundary conditions used in the modeling will be given in section 4.

The change of phase from liquid to solid is described mathematically by the following phase conditions

$$T_l(S, t) = T_s(S, t) = T_m , \quad (5a)$$

$$\kappa_l \nabla T_l \cdot \hat{\mathbf{n}} - \kappa_s \nabla T_s \cdot \hat{\mathbf{n}} = \rho_s \Delta H (\mathbf{u}_s - \mathbf{u}_l) \cdot \hat{\mathbf{n}} , \quad (6a)$$

$$\rho_l (\mathbf{u}_l - \mathbf{u}_l) \cdot \hat{\mathbf{n}} = \rho_s (\mathbf{u}_s - \mathbf{u}_l) \cdot \hat{\mathbf{n}} , \quad (7)$$

$$(\mathbf{u}_l - \mathbf{u}_s) \times \hat{\mathbf{n}} = 0 \quad (8)$$

which need to be satisfied at the solid/liquid interface. Here subscripts, s and l , refer to the solid and liquid region, respectively; \mathbf{u}_s is the solid pulling velocity; \mathbf{u}_l is the velocity of the interface; T_m is the melting temperature; $\hat{\mathbf{n}}$ is the unit norm of the interface pointing from the liquid to the solid; ΔH is the latent heat of fusion. From physical point of view, equations (5)-(8) represent thermal equilibrium at the interface, the heat flux balance between the phases which includes latent heat release, the mass flux balance across the interface and the no-slip condition at the liquid side of the interface, respectively.

In order to include the solute (species) transport in the phase change analysis it is necessary to add two more interface conditions:

$$D_l \nabla C_l \cdot \hat{n} - D_s \nabla C_s \cdot \hat{n} = C_s(\mathbf{u}_s - \mathbf{u}_l) \cdot \hat{n} - C_l(\mathbf{u}_l - \mathbf{u}_l) \cdot \hat{n}, \quad (9)$$

$$C_s = kC_l \quad (10)$$

where k is the partition coefficient. Eqn. (9) describes the mass conservation for solute transport across the interface and eqn. (10) is actually the chemical equilibrium determined by the phase diagram. In this case the melting temperature depends on solute concentration and condition (5a) becomes

$$T_l = T_s = T_m(C) = T_A + mC_l \quad (5b)$$

where T_A is a constant and

$$m = m(C) \equiv \frac{dT_m}{dC} \quad (11)$$

is the rate of change of the melting temperature with respect to C . Note that the model summarized in this section assumes a sharp solid/liquid interface and the problem will be solved by the interface tracking approach with deformable grids.

3.2 Non-Dimensionalization

It is well known that non-dimensional formulation renders many advantages for studying the physical problems. Scaling the fundamental variables with respect to their characteristic values and defining dimensionless parameter groups provide a measure of the relative importance of the various terms in the governing equations and identifies the dominant physical phenomena. For nonlinear problems, non-dimensionalization can also help ease the convergence difficulties in the nonlinear iterative solution process. For these reasons, the non-dimensional formulation is also used in this work, especially for the cases when the nonlinearity is high as well as for the parametric and asymptotic analysis.

To non-dimensionalize the momentum equation, we first choose a characteristic velocity U and a characteristic length L . Then we define the following dimensionless variables

$$\left. \begin{aligned} \mathbf{u}^* &= \mathbf{u}/U, & \mathbf{x}^* &= \mathbf{x}/L \\ p^* &= p/(\rho_0 U^2), & t^* &= tU/L \\ T^* &= (T - T_0)/\Delta T, & \mu^*(T^*) &= \mu(T)/\mu_0 \\ \beta_T^* &= 1, & \beta_c^* &= \beta_c/(\beta_T \Delta T) \end{aligned} \right\} \quad (12)$$

Substituting (12) into (1a) and introducing the non-dimensional parameters summarized in Table 2 leads to the following non-dimensional equation of motion

$$\left(\frac{\partial \mathbf{u}^*}{\partial t^*} + \mathbf{u}^* \cdot \nabla^* \mathbf{u}^* \right) = -\nabla^* p^* + \frac{1}{\sqrt{Gr}} \nabla^* \cdot \{ \mu^*(T^*) [\nabla^* \mathbf{u}^* + (\nabla^* \mathbf{u}^*)^T] \} + \quad (1b)$$

$$+ \frac{1}{\beta_T \Delta T} \mathbf{e}_g - (\beta_T^* T^* + \beta_c^* C) \mathbf{e}_g + \frac{Ha^2}{\sqrt{Gr}} (\mathbf{u}^* \times \mathbf{e}_B) \times \mathbf{e}_B$$

in which \mathbf{e}_g and \mathbf{e}_B are unit vectors of gravity and magnetic field.

Dimensionless Number	Definition	Range of Value
Reynolds No.	$Re = \rho_0 U L / \mu_0$	8.5 ~ 850
Grashof No.	$Gr = \rho_0^2 \beta_T \Delta T g L^3 / \mu_0^2$	72 ~ 72×10^4
Hartman No.	$Ha = BL \sqrt{\sigma_m / \mu_0}$	258 (5T)
Thermal Peclet No.	$Pe_T = UL / \alpha_0$	0.91 ~ 91
Prandtl No.	$Pr = \mu_0 c_p / \kappa_0$	0.107
Thermal Rayleigh No.	$Ra_T = \rho_0 g \beta_T \Delta T L^3 / \mu_0 \alpha_0$	$7.7 \sim 7.7 \times 10^4$
Stefan No.	$St = \Delta H / c_p \Delta T$	3.327
Schmidt No.	$Sc = \mu_0 / \rho_0 \alpha_c$	31.56
Solute Peclet No.	$Pe_c = UL / \alpha_c$	$2.7 \sim 2.7 \times 10^4$
Solute Rayleigh No.	$Ra_c = \rho_0 g \beta_c C_0 L^3 / \mu_0 \alpha_0$	$12 \sim 12 \times 10^4$

Table 2 Non-Dimensional parameter groups and their typical ranges of value for vertical Bridge growth of LTT under the terrestrial and microgravity conditions. The upper limit is for 1g and the lower bound corresponds to $10^{-4}g$. The characteristic velocity used here is based on the natural convection, i.e. $U = \sqrt{\beta_T \Delta T g L}$, where $\Delta T = T_h - T_m \approx 250^\circ C$. The characteristic length is the radius of ampoule, $R = 0.5\text{cm}$, which is different from the definition used in [19]. If the ampoule length, $L = 11\text{cm}$ is used then some of the numbers will have much higher values. For instance, Ra_T will become as high as 8.2×10^8 .

For heat transport, we have the following non-dimensional energy equation

$$\frac{\partial T^*}{\partial t^*} + \mathbf{u}^* \cdot \nabla^* T^* = \frac{1}{Pe_T} \nabla^* \cdot [\alpha^*(T^*) \nabla^* T^*] \quad (3c)$$

Here the thermal diffusivity $\alpha^*(T^*)$ is assumed be a function of temperature and is scaled by a reference value α_0 . For constant thermal diffusivity, $\alpha^* \equiv 1$. The dimensionless

convective heat transfer boundary condition reads

$$Q^* = h_c^*(T^* - T_c^*) \quad (13a)$$

where

$$Q^* \equiv -\frac{\kappa^*}{Pe_T} \frac{\partial T^*}{\partial n^*}, \quad h_c^* = \frac{L}{k_0 Pe_T}, \quad T_c^* = \frac{T_c - T_0}{\Delta T} \quad (13b)$$

and the Stefan condition becomes

$$Q_s^* - Q_l^* = \Delta H^*(u_s^* - u_l^*) \cdot \hat{n} \quad (6b)$$

where the dimensionless latent heat is given by

$$\Delta H^* = \frac{\rho_s}{\rho_0} \cdot \frac{1}{Ste} \quad (6c)$$

Similarly, we have the following non-dimensional balance equation for concentration

$$\frac{\partial C}{\partial t^*} + \mathbf{u}^* \cdot \nabla^* C = \frac{1}{Pe_c} \nabla^* \cdot (\alpha_c^* \nabla^* C) \quad (4b)$$

Note that C is already dimensionless and $\alpha_c^* = \alpha_c/\alpha_c^0$ is the non-dimensional solute diffusivity. If $\alpha_c \equiv \alpha_c^0$ is a constant, then α_c^* reduces to 1. The mass transfer boundary condition is transformed to

$$q_m^* = h_m C \quad (14a)$$

where

$$q_m^* \equiv -\frac{\alpha^*}{Pe_c} \frac{\partial C}{\partial n^*}, \quad h_m^* = \frac{L}{\rho \alpha_0 Pe_c} \quad (14b)$$

and the phase change condition (liquidus) becomes

$$T^* = T_m^* + m^* C \quad (5b)$$

where $T_m^* = (T_m - T_0)/\Delta T$ and $m^* = m/\Delta T$.

3.3 Pseudo-Steady-State Model

To simulate the steady growth of LTT in the vertical and horizontal Bridgman configurations, the so-called *pseudo-steady-state model* (PSSM) [5,19] is adopted in the present work. In PSSM, the directional steady movement of the solid/liquid interface during the steady growth is modeled by letting melt enter at its hot end with a uniform growth velocity V_g and composition C_0 and by removing the crystal from the cold end at a speed

that conserves the mass of the alloy in the system. Note that as a simplification of the real growth condition the PSSM neglects the transient effects in the field variables (such as velocity, pressure, temperature and concentration, etc.) caused by the steady decrease of the length of the melt during crystal growth and the displacement of the ampoule in the furnace. This simplification is valid for long ampoules and melts with low Prandtl numbers, in which the transient effects on heat transfer are small [40]. It is also known that for sufficiently long ampoules the thermal end effects are negligible [41].

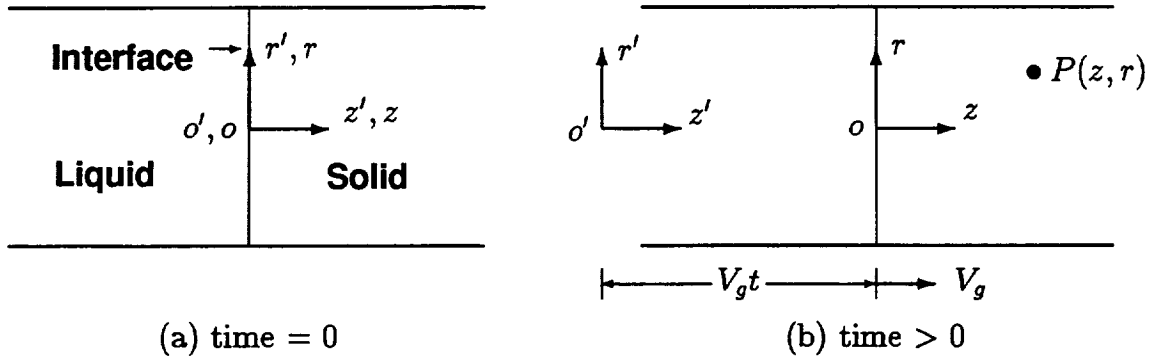


Figure 2 Definition of the moving coordinate system zor used in the PSSM and its relation with a reference frame $z'o'r'$ fixed in space.

Perhaps the most important feature of PSSM is the application of the moving coordinate system. In this work, the moving coordinate system is introduced by fixing its origin at the center of the moving solid/liquid interface. Fig. 2 shows the definition of the moving coordinate system and its relation with a fixed frame in space. Let zor denote the moving coordinate system for the axi-symmetric case and $z'o'r'$ a fixed coordinate system in space, respectively. We choose the origins of the two systems to coincide at time equals zero, as depicted in Fig. 2(a). At $t > 0$, the coordinates of point P in the moving coordinate system are (r, z) while its coordinates with respect to a stationary observer sitting on the fixed frame are (r', z') . From Fig. 2(b), it is evident that

$$\begin{aligned} r &= r' \\ z &= z' - V_g t \end{aligned} \tag{12}$$

Here V_g is the growth rate with $V_g > 0$ corresponding to melting and $V_g < 0$ to solidification.

The relation of velocity in the two systems can be easily derived by considering the time derivatives of (12), namely

$$\dot{r} = \dot{r}' \quad \Rightarrow \quad u_r = u_r' \tag{13}$$

$$\dot{z} = \dot{z}' - V_g \Rightarrow u_z + V_g = u'_z \quad (14)$$

According to (13) the r -components of velocity in the two systems are identical. Since the s/l interface becomes stationary in the moving coordinate system, the steady movement of the interface is now represented by the translation of the moving coordinate system in an opposite direction to the growth (or melt) direction. The translation of the moving coordinate system does affect the z -component of velocity. Equation (14) indicates that although the material particle in the solid is stationary with respect to the fixed coordinate system, it has a constant translation velocity when viewed from the moving coordinate system. Consequently, the velocity boundary conditions for u_z need to be modified in the moving coordinate system. Let $\bar{\varphi}$ denote the given velocity on boundary Γ'_u in the fixed coordinate system, viz.

$$u'_z = \bar{\varphi}(r', z') . \quad (15)$$

Then the velocity boundary condition in the moving coordinate system becomes

$$u_z = \bar{\varphi}(r, z) - V_g . \quad \forall (r, z) \in \Gamma_u \quad (16)$$

For instance, at the no-slip boundary $\bar{\varphi} \equiv 0$, but under system *zor* eqn. (16) gives $u_z = -V_g$, which is due to the translation of the moving coordinate system.

In order to obtain the transformed governing equations in the moving coordinate system, we also need to consider the spatial derivatives. By using the chain-rule, it is easy to verify the following relation for the first-order spatial derivatives

$$\begin{aligned} \frac{\partial}{\partial r'} &= \frac{\partial}{\partial r} \frac{\partial r}{\partial r'} = \frac{\partial}{\partial r} \\ \frac{\partial}{\partial z'} &= \frac{\partial}{\partial z} \frac{\partial z}{\partial z'} = \frac{\partial}{\partial z} \end{aligned} \quad (17)$$

And likewise for the second-order derivatives we have

$$\frac{\partial^2}{\partial r'^2} = \frac{\partial^2}{\partial r^2}, \quad \frac{\partial^2}{\partial z'^2} = \frac{\partial^2}{\partial z^2} \quad (18)$$

Eqns. (17) and (18) suggest that the spatial derivatives in the governing equations are unaffected under the coordinate transformation. Applying (12)-(14) and (18) in eqn. (3), the transient energy equation is now reduced to the following steady state form under the moving coordinate system

$$\rho_0 c_p (\mathbf{u} + \mathbf{V}) \cdot \nabla T = \nabla \cdot (\kappa \nabla T) . \quad (3b)$$

Here \mathbf{V} is the translation velocity vector of the moving coordinate system.

3.4 Special Treatment for Concentration

The special difficulty in solving mass transfer in phase-change problems is the discontinuity of solute concentration itself across the interface, as indicated by interface condition (10). Furthermore, the melting temperature is no longer a constant, instead it has to be determined by the local solute concentration. However in the standard FEM formulation, both the trial and test function have to be at least C^0 continuous and no jump is allowed for the primitive variables. Therefore a special treatment is necessary for the species equation.

To eliminate the discontinuity of C at the interface, the following transformation

$$C_s^* = C_s/k \quad (19)$$

is performed for concentration in the solid region. The interface condition (10) is then reduced to

$$C_l = C_s^* \quad (20)$$

and thus C becomes continuous across the phase change interface. It can be proved [30] that the mass flux balance condition (9) can be rewritten in the following form

$$(D_l \nabla C_l - D_s \nabla C_s) \cdot \hat{\mathbf{n}} = h_c C_l \quad (21)$$

where the coefficient

$$h_c = \rho_s(1-k)(\mathbf{u}_s - \mathbf{u}_l) \cdot \hat{\mathbf{n}} + D_s(1-k)\hat{\mathbf{n}} \cdot \nabla C_s^*/C_l. \quad (22)$$

The second term in (22) involves spatial gradient of concentration at the solid side. Since the solute diffusivity in solids, i.e. D_s , is usually several orders of magnitude smaller than D_l , it is reasonable to assume this term is negligible. In our computation, the interface condition (21) is imposed through a species transfer boundary element at the moving interface.

3.5 Dimensional Units for the Lorentz Force Term

When the dimensional form of the momentum equation is used in the magnetic damping analysis, it is important to have the units of the Lorentz body force term to be dimensionally consistent with the other terms in the same equation. It is easy to verify that the other terms in equation (1a) have the following general units

$$\rho_0 \frac{\partial \mathbf{u}}{\partial t} \sim \frac{\text{force}}{\text{volume}}. \quad (23)$$

For the standard international (SI) unit system, all the units involved in the Lorentz force term are clearly defined, such as the following definitions for the magnetic field strength and the electrical conductivity

$$B \sim T \text{ (Tesla)} = \frac{N}{A \cdot m} \quad (24)$$

$$\sigma_m \sim \frac{1}{\Omega \cdot m} = \frac{A^2 \cdot s}{N \cdot m^2} \quad (25)$$

where A is electric current in amperes, Ω is resistance in ohms and N is force in Newtons. Note that the following relations: $\Omega = V/A$, $V = W/A$ and $W = N \cdot m/s$ are used in deriving (25). By using (24) and (25) we can easily confirm the SI units of the Lorentz force term, i.e.

$$\sigma_m B^2 U \sim \frac{A^2 \cdot s}{N \cdot m^2} \left(\frac{N}{A \cdot m} \right)^2 \frac{m}{s} = \frac{N}{m^3} \quad (26)$$

which is indeed consistent with general units (23) of the other terms.

However, for the centimeter-gram-second (CGS) unit system, things are not so straightforward. This is because there are no CGS units commonly used for voltage, current, etc. In this case, we need to consider the following term

$$\frac{\sigma_m}{\rho_0} B^2 = \alpha_m B^2 \quad (27)$$

where $\alpha_m \equiv \sigma_m / \rho_0$ is called the mass diffusivity in FIDAP. Then we introduce the following result

Proposition: *The dimensional unit of (27) is invariant for both the SI and the CGS unit systems.*

Proof: Substituting the SI units for σ_m , ρ_0 and B into (27) gives

$$\frac{\sigma_m}{\rho_0} B^2 \sim \frac{A^2 \cdot s}{N \cdot m^2} \frac{m^3}{kg} \left(\frac{N}{A \cdot m} \right)^2 = \frac{s \cdot N}{kg \cdot m} = \frac{1}{s} \quad (28)$$

which is the same in the two unit systems.

To confirm the above results, we substitute (28) into the Lorentz force term and obtain

$$\rho_0 \alpha_m B^2 U \sim \frac{g}{cm^3} \frac{1}{s} \frac{cm}{s} = \frac{dyne}{cm^3} \quad (29)$$

which is exactly the consistent unit for the CGS unit system. Therefore, the above results suggest that for magnetic damping analysis based on the CGS units, one can use a mixed units in the Lorentz force term, namely use SI units for the magnetic field related term (27) while inputting the rest of the quantities in the Lorentz force term with CGS units. The CGS units of the Lorentz force term will then be consistent with the other terms in the momentum equation.

4. NUMERICAL SIMULATION

4.1 The FEM Model

In this paper we consider two Bridgman growth configurations. The first is the bottom seeded (vertical) Bridgman growth. In this configuration the hot (melt) zone is on the top and the cold (crystal) zone is at the bottom. The furnace axis is parallel to the gravity vector which is in the vertical direction pointing downwards. For axisymmetric boundary conditions it is reasonable to assume that the heat, species and flow fields are all axisymmetric, i.e. independent of the θ -coordinate. Therefore a simplified axisymmetric model, as depicted in Fig. 3, is used to model the vertical Bridgman growth. The computational boundary conditions imposed for the energy, momentum and species equations are summarized in Figure 4. For the momentum equation, we specify the no-slip conditions on the surface between the sample and ampoule wall. For heat transport we impose the measured thermal conditions on the outer surface of the ampoule. As shown in Fig. 4(b), the thermal profile on the ampoule surface consists of the hot, adiabatic and cold zones. The concentration boundary conditions are shown in Fig. 4(c).

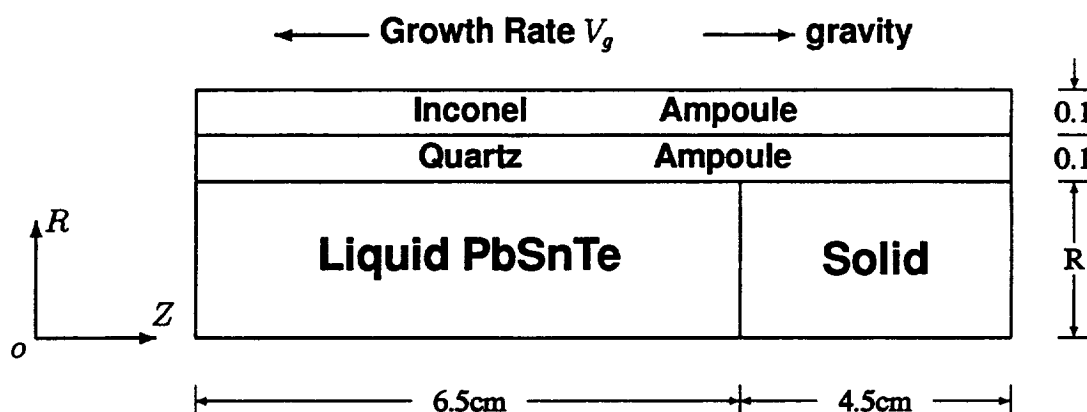
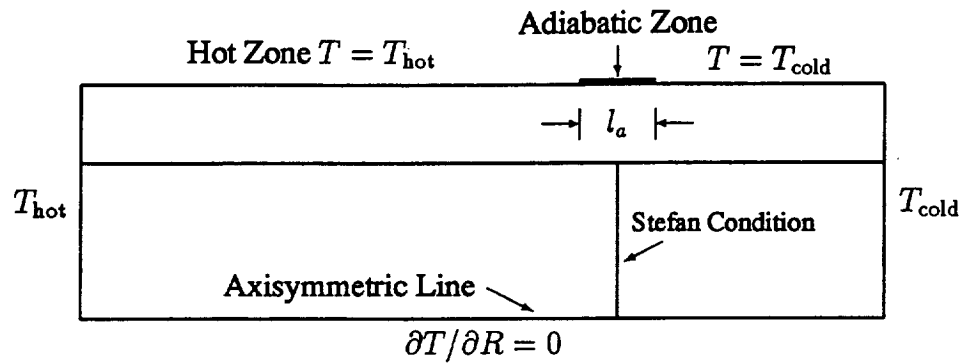
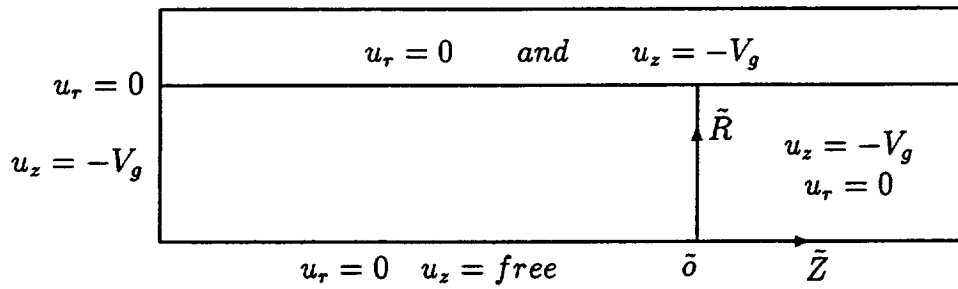


Figure 3. Schematic diagram and geometric definitions of a simplified axisymmetric FEM model for the vertical Bridgman growth configuration.

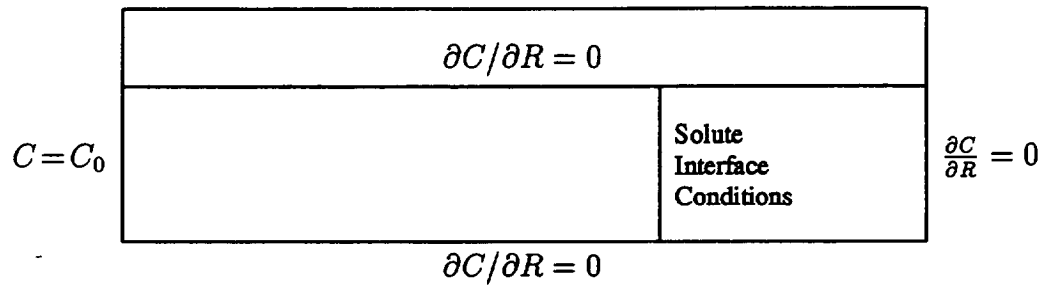
The second configuration is the horizontal Bridgman in which the gravity vector is perpendicular to the furnace axis (i.e. the z -axis defined in Fig. 3). In this case the solutions are assumed to be symmetric about the vertical center plane and an idealized two-dimensional model is used to simulate this center plane. Although this 2-D model is just a simplification for the real situation, we hope it can provide at least some qualitative



(a) Thermal Boundary Conditions



(b) Velocity Boundary Conditions for Pseudo-Steady State Analysis



(c) Boundary Conditions for Solute Concentration

Figure 4. Computational boundary conditions used for the axisymmetric model.

information for this growth configuration. More accurate modeling will rely on the full three-dimensional model which is currently under development.

4.2 The Front Tracking Approach

The most challenging difficulty posed by phase change problems is the moving solid-liquid interface whose position is usually an unknown function of time and space and needs to be determined as a part of the solution. In the literature various numerical techniques have been proposed to deal with the moving interface for phase change problems [42]. Among them, two main classes of methods can be distinguished, namely the fixed-grid enthalpy methods and the front-tracking methods. The front-tracking technique with deforming mesh is used in our modeling.

Unlike the enthalpy method, the phase change front tracking method can model the phase change problems with a sharp (single) solid/liquid interface. The front tracking approach used in this work involves a deformable spatial mesh in which nodes located on the interface are allowed to move such that they remain on the moving boundary. For each node on the moving interface, an additional degree of freedom is introduced. This new degree of freedom determines directly the position of the node in space and is an integral part of the representation of the moving interface.

To update the interface position and remesh the interior domains, a method of spines is used. It is a generalization of the method developed by Saito and Scriven [43], in which the moving nodes lie on and the interface movement is guided by the generator lines called *spines*. In particular, the position of the moving node is represented parametrically by

$$\begin{aligned} x_i &= \alpha_x[h_{j+1} + \omega t_i(h_j - h_{j+1})] + \beta_x \\ y_i &= \alpha_y[h_{j+1} + \omega t_i(h_j - h_{j+1})] + \beta_y \\ z_i &= \alpha_z[h_{j+1} + \omega t_i(h_j - h_{j+1})] + \beta_z \end{aligned} \quad (30)$$

where h_j is the interface location parameter for a given spine, $(\alpha_x, \alpha_y, \alpha_z)$ is the direction vector, $(\beta_x, \beta_y, \beta_z)$ is the base point of the spine. The location (x_i, y_i, z_i) of the moving node on the spine is determined from its relative position, ωt_i , to the moving interfaces located at h_j and h_{j+1} . Here h_j are the new degree of freedom introduced.

For steady state problems, applying Galerkin's formulation and the standard discretization procedure to the momentum equation (1) results in a nonlinear algebraic system in the following matrix form [28]

$$\mathbf{A}(\mathbf{U})\mathbf{U} + \mathbf{K}(\mathbf{T}, \mathbf{U}) - \mathbf{C}\mathbf{P} + \mathbf{B}\mathbf{X} = \mathbf{F} \quad (31)$$

where \mathbf{X} is the global vector of the moving interface unknowns, $\mathbf{A}(\mathbf{U})$ accounts for contribution from the convective terms, $\mathbf{K}(\mathbf{U})$ includes the diffusive terms, \mathbf{C} is the divergence matrix, \mathbf{B} represents the contribution of the normal stress balance condition at boundary, \mathbf{F} is a body force vector.

4.3 The Segregated Solver

System (31) along with the energy equation, species equation and other interface and boundary conditions are solved by a segregated solution procedure. In contrast to the traditional fully coupled approach (such as the Newton-type solver), the segregated solution algorithm does not form the global system matrix directly. Instead, it decomposes the global system matrix into smaller sub-matrices each governing the nodal unknowns associated with only one conservation equation. These segregated sub-matrices are then solved in a sequential manner. Since the storage of the individual sub-matrices is considerably less than that needed to store the global system matrix, the storage requirements of the segregated approach are substantially less than those of the fully coupled approach.

4.4 Numerical Solution

The axisymmetric and 2-D FEM models are built with the 4-node bilinear element, in which velocity, temperature and species are approximated by bilinear shape functions. The pressure is approximated as piecewise constant.

In this work numerical solutions are obtained by using a modified version of the finite element program FIDAP. The details of the FEM formulation in FIDAP are documented in [28]. The nonlinear iteration termination is controlled by a specified tolerance of 10^{-3} for the relative error norms of velocity, residual and free surface update.

5. BENCHMARK TESTS

Due to the complexity of the crystal growth problem considered herewith, there exists no closed-form (analytical) solution, nor adequate published results in the literature. Therefore, it is necessary to conduct a series of benchmark tests to check the validity of the numerical model and the accuracy of the numerical solutions. In this section we summarize some of the typical tests that have been performed. These test problems are usually simplified so that analytical solutions are available for quantitative comparisons. Each simple test is aimed to examine only a particular part of the model.

5.1 1-D Crystallization of A Binary Alloy

First, we consider the classical 1-D solidification of a binary alloy in a semi-infinite region, $x > 0$. Initially the whole block of molten alloy is in liquid phase with uniform initial temperature and concentration distributions, T_0 and C_0 . At $t = 0^+$, the temperature at the left end surface, $x = 0$, is lowered to $T_1 < T_m$. Hence crystallization of the mixture is initiated at the boundary $x = 0$. The complete mathematical formulation for this problem can be found in [44]. The main objective of this test is to verify the formulation and FEM implementation related with concentration, phase change conditions and front tracking.

Under certain assumptions, such as constant conduction and diffusion coefficients in each phase, this problem admits a similarity solution which is usually referred to as *Rubinstein solution* and has the following general form

$$\begin{aligned}
 S &= 2\beta\sqrt{t} \\
 C_s &= -k_s T_m \\
 T_s &= T_1 + (T_m - T_1) \operatorname{erf}\left(\frac{x}{2a_s\sqrt{t}}\right) / \operatorname{erf}\left(\frac{\beta}{a_s}\right) \\
 C_l &= C_0 - (k_l T_m + C_0) \operatorname{erfc}\left(\frac{x}{2\sqrt{D_l t}}\right) / \operatorname{erfc}\left(\frac{\beta}{\sqrt{D_l}}\right) \\
 T_l &= T_0 + (T_m - T_0) \operatorname{erfc}\left(\frac{x}{2a_l\sqrt{t}}\right) / \operatorname{erfc}\left(\frac{\beta}{a_l}\right)
 \end{aligned} \tag{5.1}$$

Here $S(t)$ is the interface position, a is thermal diffusivity, erf is the *error function* and erfc is the *complementary error function*. This solution presumes a linearized liquidus and solidus

$$C_s = -k_s T_m, \quad C_l = -k_l T_m \tag{5.2}$$

for concentrations at the solid side and the liquid side of the interface, respectively. k_s and k_l are the constant slopes of the straight liquidus and solidus lines.

There are two unknown parameters, namely β and T_m , in the above solution. They need to be determined through the heat and mass flux balance conditions at the interface. The two interface conditions form a system of two transcendental equations

$$\rho \Delta H \beta = \frac{\kappa_s (T_m - T_1) e^{-\beta^2/a_s^2}}{a_s \sqrt{\pi} \operatorname{erf}(\beta/a_s)} + \frac{\kappa_l (T_m - T_0) e^{-\beta^2/a_l^2}}{a_l \sqrt{\pi} \operatorname{erfc}(\beta/a_l)} \tag{5.3}$$

$$(k_s - k_l) T_m \beta = -\sqrt{\frac{D_l}{\pi}} \frac{k_l T_m + C_0}{\operatorname{erfc}(\beta/\sqrt{D_l})} e^{-\beta^2/D_l} \tag{5.4}$$

It can be proved that there exists a solution for this system. Eqns. (5.3) and (5.4) can be solved simultaneously or further reduced to a single transcendental equation

$$\left\{ a_l \left[\sqrt{\pi} \rho \Delta H \beta a_s \operatorname{erf} \left(\frac{\beta}{a_s} \right) + T_1 \kappa_s e^{-\beta^2/a_s^2} \right] \operatorname{erfc} \left(\frac{\beta}{a_l} \right) e^{\beta^2/a_l^2} + T_0 \kappa_l a_s \operatorname{erf} \left(\frac{\beta}{a_s} \right) \right\} \cdot$$

$$\left[\sqrt{\pi} (k_s - k_l) \beta \operatorname{erfc} \left(\frac{\beta}{\sqrt{D_l}} \right) + \sqrt{D_l} k_l e^{-\beta^2/D_l} \right] +$$

$$+ \sqrt{D_l} C_0 e^{-\beta^2/D_l} \left[\kappa_s a_l e^{-\beta^2/a_s^2 + \beta^2/a_l^2} \operatorname{erfc} \left(\frac{\beta}{a_l} \right) + \kappa_l a_s \operatorname{erf} \left(\frac{\beta}{a_s} \right) \right] = 0 \quad (5.5)$$

which determines β . Then T_m is given by

$$T_m = \frac{-\sqrt{D_l} C_0 e^{-\beta^2/D_l}}{\left[\sqrt{\pi} (k_s - k_l) \beta \operatorname{erfc}(\beta/\sqrt{D_l}) + \sqrt{D_l} k_l e^{-\beta^2/D_l} \right]}. \quad (5.6)$$

In our test we consider a special case in which the following values are chosen for the parameters involved, viz.

$$\begin{aligned} \rho &= 1, & \Delta H &= 1 \\ \kappa_s &= \kappa_l = 1 \\ D_s &= 1, & D_l &= 1/2 \\ a_s &= a_l = 1 \\ k_s &= 1, & k_l &= 2 \\ T_0 &= 1, & T_1 &= -1, & C_0 &= 0.1. \end{aligned} \quad (5.7)$$

Substituting (5.7) into (5.5) and (5.6) and solving the nonlinear equations give

$$\beta = 0.3526943389 \quad \text{and} \quad T_m = -0.06872222638. \quad (5.8)$$

Numerical solution is obtained by using FIDAP. Only a finite part of the semi-infinite domain, i.e. $[0,4]$, is considered. The boundary conditions imposed for energy equation are of mixed type with a constant temperature $T_1 = -1$ at $x=0$ and a no-flux ($\partial T/\partial x=0$) condition at $x=4$. For concentration, the no-flux condition ($\partial C/\partial x=0$) is applied to both end surfaces. To avoid problems associated with initiation at $t=0$, numerical solution begins from $t=0.1$ with the initial T and C provided by the similarity solution (5.1). The backward Euler time integration scheme is used with a time step $\Delta t=0.01$ and the solution ends at $t=0.4$. Comparisons are made between the numerical solution and the similarity solution. Some typical results are shown in Fig. 5. As we can see the agreement is excellent and the error is within 1%.

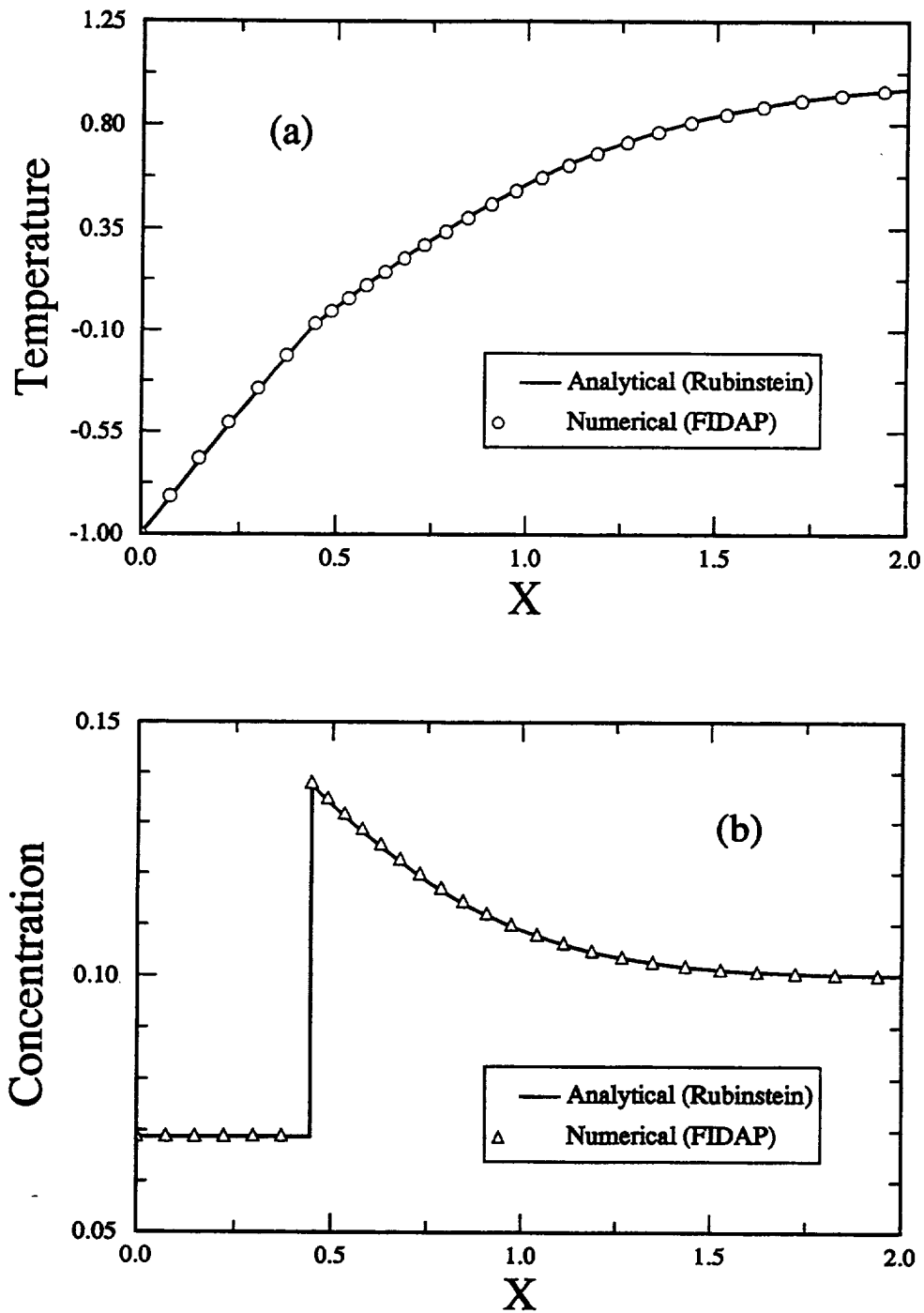


Figure 5. Comparison of numerical solution with the similarity solution for the 1-D solidification test problem. The solution shown is calculated at $t = 0.4$

5.2 Axi-Symmetric Poiseuille Flow Subject to Buoyancy Force

This simple test is designed for checking the formulation and FEM implementation on the buoyancy force term in the momentum equation. For simplicity, we assume a constant change in temperature and concentration which in turn leads to a constant buoyancy body force

$$\rho_0(1 - \beta_T \Delta T - \beta_c \Delta C)g .$$

Consider a rectangular domain in the axi-symmetric plane with length L and radius R_0 . The boundary conditions for the momentum equation are imposed as

$$\begin{aligned} u_r &= 0, & \partial u_z / \partial r &= 0 & @ r &= 0 \\ u_r &= 0, & \sigma_z &= -\Delta p, & @ z &= 0 \\ u_r &= 0, & u_z &= 0, & @ r &= R_0 \\ u_r &= 0, & \sigma_z &= 0 . & @ z &= L \end{aligned} \quad (5.9)$$

Furthermore we assume laminar flow and the only non-zero velocity component is $u_z = u(r)$. For this test problem, the analytical solution can be easily derived and u_z has the following form

$$u(r) = \frac{1}{4\mu} \left[\rho_0(1 - \beta_T \Delta T - \beta_c \Delta C)g - \frac{\partial p}{\partial z} \right] (R_0^2 - r^2) \quad (5.10)$$

where $\partial p / \partial z$ is the pressure gradient. The following data are used in our test

$$\begin{aligned} R_0 &= 0.5, & L &= 1.0 \\ \rho_0 &= 2, & \mu &= 2 \\ \beta_T &= 0.002, & \beta_c &= -0.1 \\ \Delta T &= 100, & \Delta C &= 1 \\ g &= 0.5, & \partial p / \partial x &= -\Delta p = -0.8 . \end{aligned} \quad (5.11)$$

The above data lead to a maximum velocity

$$u_{\max} = u(0) \approx 0.053125 . \quad (5.12)$$

The problem is solved by using the bilinear element. To observe the convergence of numerical solution, we start from a coarse mesh with an element size $\Delta x_1 = 0.1$. We then refine the mesh by dividing the square element by half in both coordinate directions. Namely, the subsequent meshes have element sizes $\Delta x_2 = \Delta x_1 / 2$ and $\Delta x_3 = \Delta x_1 / 4$. A

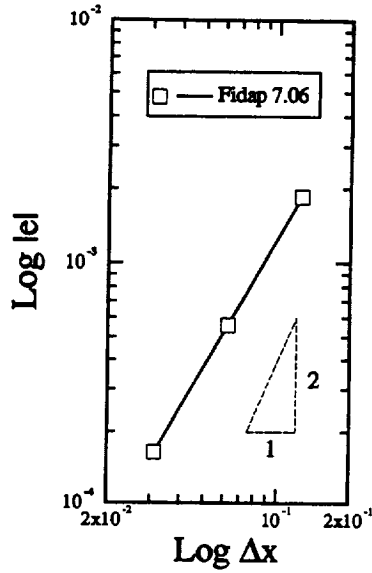


Figure 6. The convergence check for FEM solution of u_{\max} at $r=0$ for the axis-symmetric Poiseuille flow test problem. The error norm is defined as $|e| \equiv |u_{\max}^h - \bar{u}_{\max}|$, where u_{\max}^h is mesh dependent FEM solution and \bar{u}_{\max} is the analytical solution.

verification of the pointwise convergence of u_{\max} is presented in Fig. 6. The slope of the curve in Fig. 6 indicates a second-order convergence rate for velocity solution, which agrees well with the FEM theory [45].

5.3 Couette Flow in A Vertical Magnetic Field

This test is designed for validating the formulation related with magnetic damping. Consider the plate-driven simple shearing flow of a Newtonian fluid shown in Fig. 7. The flow is subject to a uniform vertical magnetic field. Assume the electric field is everywhere equal to zero, the magnetic induction is not distorted by the fluid flow, the magnetic field is equal to the imposed value and the buoyancy force term is negligible.

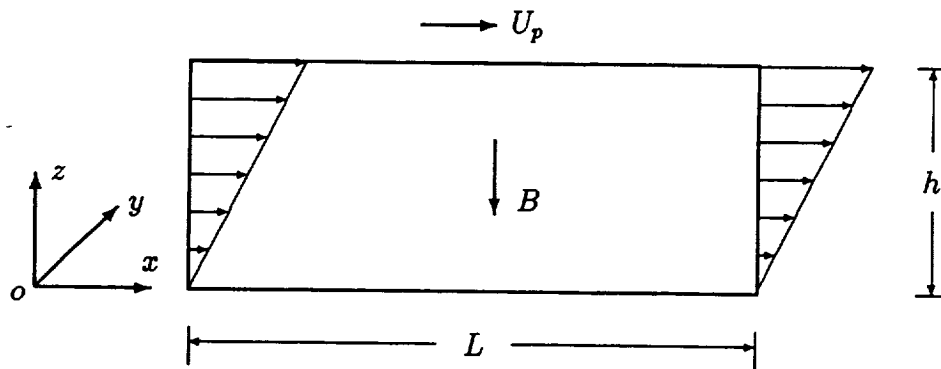


Figure 7. Plate-driven Couette flow before being subject to a uniform transverse magnetic field. Definition of the problem.

In this case, the Lorentz body force is simplified to

$$\sigma_m(\mathbf{u} \times \mathbf{B}) \times \mathbf{B} = -\sigma_m u_x B^2 \mathbf{i} \quad (5.13)$$

which acts in the opposite direction to the motion of fluid. Therefore the effect of Lorentz force is to reduce the x -component of velocity. Solving the momentum equation with the appropriate boundary conditions we obtain the following analytical solution in nondimensional form

$$u_x = \frac{\sinh(Haz)}{\sinh(Hah)} U_p, \quad u_y = u_z = 0 \quad (5.14)$$

where Ha is the Hartman number.

The effect of magnetic damping can be seen more clearly by a very simple asymptotic analysis. Consider the limit when Ha becomes very large. It is easy to verify the following result

$$\lim_{Ha \rightarrow \infty} u_x = \lim_{Ha \rightarrow \infty} e^{-Ha(h-z)} U_p \rightarrow 0 \quad \forall z < h \quad (5.15)$$

which suggests that when the magnetic field is strong enough the velocity can be diminished everywhere in the domain except on the top plate where the above limit approaches U_p , the moving speed of the plate. Here the effect of the imposed magnetic field is in general similar to the effect of increasing the viscosity of the melt. However, care must be taken in making analogy between the so-called “*magnetic viscosity*” with the real viscosity. In some aspects, they are quite different. For example, the magnetic viscosity is anisotropic and its value depends on the magnitude of the effective velocity component, while the viscosity of a Newtonian liquid is isotropic and independent of velocity.

Due to the continuity of u_x , a boundary layer is formed near the top plate and its thickness decreases with increase of Ha . This boundary layer is very similar to the so-called Hartman boundary layer in the solidifying melt analyzed in [19]. Therefore this test problem can also examine how well the thin boundary layer can be resolved in the numerical solution.

In our test the following values are selected for the nondimensional parameters involved in (5.14).

$$h = 1, \quad U_p = 1, \quad Ha = \sqrt{2}, 10, 50. \quad (5.16)$$

The problem is solved by using the 8-node 3-D brick element in FIDAP. A total of three meshes are used with the element sizes $\Delta x_1 = 1/6$, $\Delta x_2 = 1/12$ and $\Delta x_3 = 1/24$. A typical posterior error analysis based on the three-mesh extrapolation is provided in Table 3. The

Location	Δx_1	Δx_2	Δx_3	$\Delta x=0$	Analitical
$x=1/6$.122772	.122896	.122927	.122936	.1229367
$x=1/3$.252429	.252659	.252716	.252734	.2527349
$x=1/2$.396241	.396540	.396614	.396638	.3966391
$x=2/3$.562272	.562579	.562656	.562680	.5626810
$x=5/6$.759832	.760054	.760109	.760127	.7601279

Table 3 Posterior error analysis on numerical solution of velocity by three-mesh extrapolation for the magnetic damping Couette flow problem with $Ha = \sqrt{2}$. Columns Δx_i , ($i = 1, 2, 3$) are the raw u_x results obtained from mesh 1 to mesh 3. The values in column $\Delta x = 0$ are caculated by a quadratic extrapolation. The analytical solution is given by (5.14).

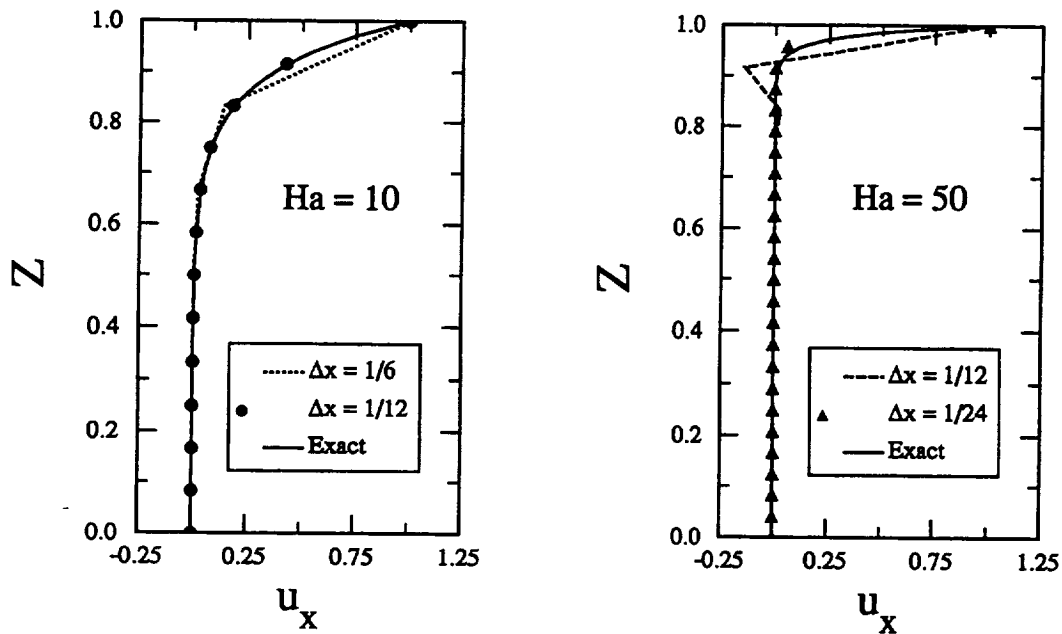


Figure 8. Numerical solutions for the magnetic damping test problem at higher Hartman numbers and comparison with analytical solution.

results indicate that the FEM solution does indeed converge at the expected second-order convergence rate with mesh refinement and the extrapolated values are accurate to the sixth digit.

To illustrate the difficulties involved with the thin boundary layer in the magnetic damping, we solve the test problem at two higher Hartman numbers and present the results in Fig. 8. As we can see, at $Ha=10$ the coarse mesh is not adequate for providing accurate results near the top boundary and one mesh refinement is necessary. When $Ha=50$, however, mesh 2 with $\Delta x_2=1/12$ becomes incapable in resolving the thin boundary layer and causes the typical numerical oscillation near the top plate. In this case a further mesh refinement is necessary in order to obtain more accurate solution. This example demonstrates clearly the importance of mesh refinement (or grading) in overcoming the numerical difficulties rendered in modeling magnetic damping.

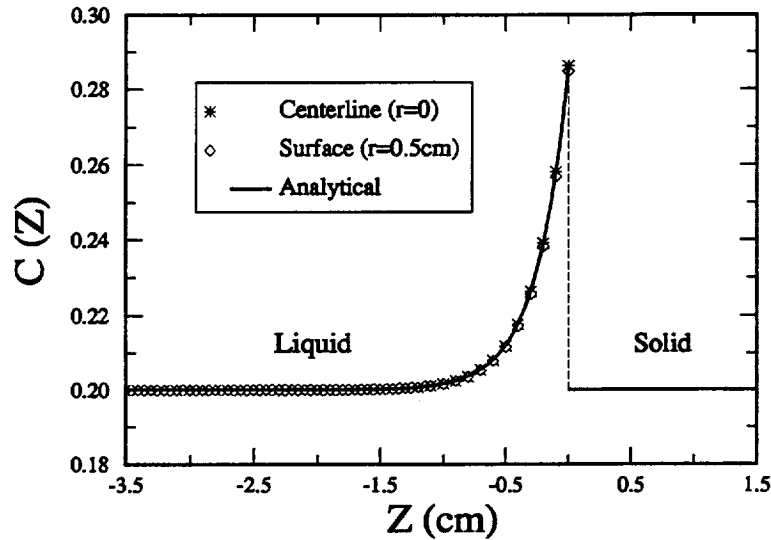


Figure 9. Numerical solution of the axial solute distribution on the centerline and surface of the LTT sample and comparison with the 1-D diffusion controlled growth solution. The FEM results are based on the axi-symmetric model for the vertical configuration with a constant growth rate $V_g = 1\text{cm/hour}$. In order to display the thin boundary layer, only a portion of the domain is shown.

5.4 Diffusion-Dominated Growth under 0g

The last test is a more realistic one and designed for testing the PSSM approach. In this test we consider the FEM model given in section 4.1 and compute the numerical

solution for an ideal growth condition with no buoyancy-induced convection. To eliminate convection, we set gravity equal zero. It is known from theory that the excess solute rejected at the moving interface will be transported by diffusion only. In this case the axial solute profile is given by the following 1-D solution [1,2]

$$C(z) = C_0 \left(1 + \frac{1-k}{k} e^{V_s z / D_l} \right) \quad \forall z \leq 0 \quad (5.17)$$

where $z = 0$ is the interface position. The initial concentration of SnTe in PbSnTe is $C_0 = 0.2\%$. The results are presented in Fig. 9. As we can see that the simulated solute boundary layer at 0g is indeed very close to the diffusion-controlled solution, and hence the validity of our numerical model has been verified.

6. VERTICAL BRIDGMAN GROWTH

Numerical simulation of Bridgman growth system involves a large number of physical and geometric parameters and the cost of each computation has forced us to focus on one set of parameters. The particular set of design parameters has been given in Table 1. The results presented in this section are therefore based on this set of parameters and the thermal profile given in Fig. 1, unless otherwise stated.

6.1 Thermal Buoyancy-Induced Convection and Its Effects on Solute Segregation

In order to study the interaction between thermal and solutal gradients, we first consider the density variation caused by thermal expansion only. In this case the thermal gradient is the main driving force for the convective flow in the melt. A thermally stable configuration (with melt on top) is used in the simulation. Here the varying parameter is the magnitude of gravity ranged from $10^{-4}g$ to $1g$, which leads to a span of thermal Rayleigh number from about 7.7 to 7.7×10^4 .

The simulated velocity fields at various gravity levels are plotted in Fig. 10a. Note that the plots shown in Fig. 10a are based on the total velocity given in (14) which includes a constant translation velocity and the buoyancy-induced convective velocity. At $10^{-4}g$ the velocity vectors shown are straight and uniform flowing toward to the interface, which indicates that the buoyancy-driven convection part of the velocity is negligibly small. At $10^{-3}g$ the convection starts to increase from the center part of the melt and streamlines become slightly curved near the interface. However, the convective velocity is still very small (about 17% of the growth rate as indicated by the value of u_{\max}). At the gravity level of $10^{-2}g$, two flow cells have formed in the melt. The smaller one near the interface is

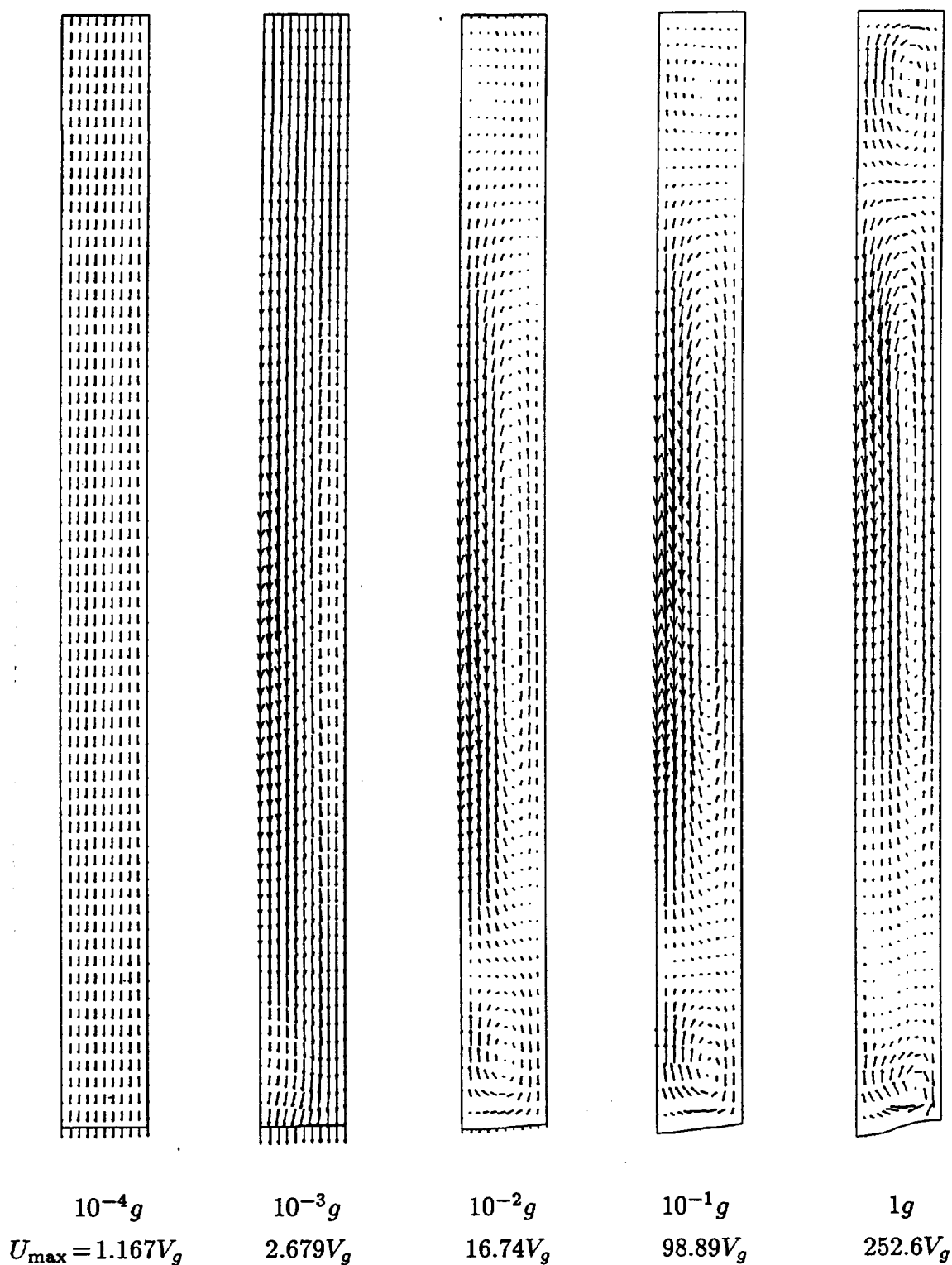


Figure 10a Vector plots of total velocity in the melt for vertical growth at various gravity levels. The buoyancy flow is induced by thermal expansion only. The left vertical boundary of each plot is the centerline of the sample and the bottom curve is the melt-crystal interface.

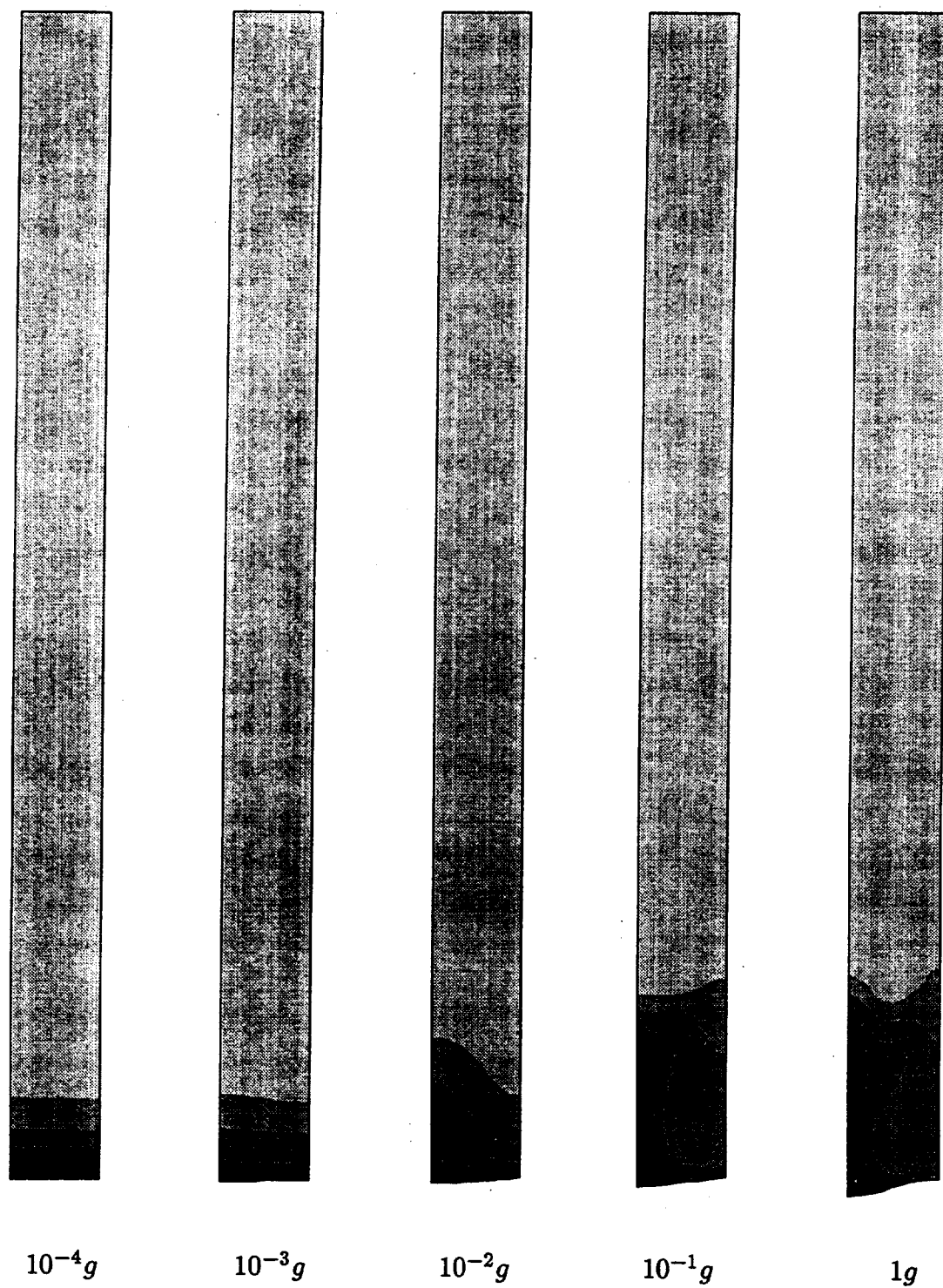


Figure 10b Solute distributions in the melt corresponding to the flow fields shown in Fig. 10a. The darker grey scale represents higher solute concentration.

driven by the radial temperature gradient. The vector direction in this smaller cell shows that the flow adjacent to the interface moves upward at the centerline of the ampoule and downward along the ampoule wall. The larger cell is driven by the axial thermal gradient caused by the transition in thermal boundary conditions from the adiabatic to hot zone. The flow direction in the larger cell is opposite to that in the smaller cell. A third flow cell is formed at $10^{-1}g$ and the overall strength of buoyancy-induced convection grows with the increase of gravity levels. The flow patterns shown in Fig. 10a are in a good qualitative agreement with that reported in the literature [19,41].

The strength of convection in the melt can be measured by the maximum velocity. The effect of different gravity levels on the convective strength in the melt can be seen more clearly from Fig. 11 in which the total maximum velocity U_{\max} versus the magnitude of gravity is plotted for the vertical growth configurations. The convective strength level marked by the horizontal dashed line in Fig. 11 is important, because at this level the buoyancy-driven convective velocity maximum is the same as the translation velocity (growth rate). It has been shown that radial segregation is often maximum when the rate of convection and growth are near equal. Therefore it can be considered as a critical point for the growth of convective strength in the melt. Let g_c denote the gravity level corresponding to this critical point. For simulated vertical growth with thermal expansion only, $g_c \approx 5 \times 10^{-4}g$. When gravity is less than g_c the convection is very weak and grows slowly with increases in g . However, when the gravity level exceeds g_c convection grows concomitantly with g and the effects of gravity on the fluid motion in the melt become significant.

It is interesting to look at the effects of thermal buoyancy-induced convection on the solute segregation. There are in general two basic forms of solute segregation, namely longitudinal (axial) macro segregation caused by complete mixing and transverse (radial) segregation caused by low levels of mixing near the interface. As analyzed by Brown et al [19], these two forms of segregation are a function of convection level in the melt. In our computation the convective strength is directly related to the magnitude of gravity. As shown in Fig. 10b, at low convective flow levels (such as $10^{-4}g$ and $10^{-3}g$) the radial segregation is negligibly small and the axial segregation is very close to the diffusion-dominated growth with a thin solute boundary layer near the interface. At $10^{-3}g$ the radial segregation starts to increase and the iso-concentration lines become curved. This is due to the small convective flow cell formed adjacent to the interface. The excess solute

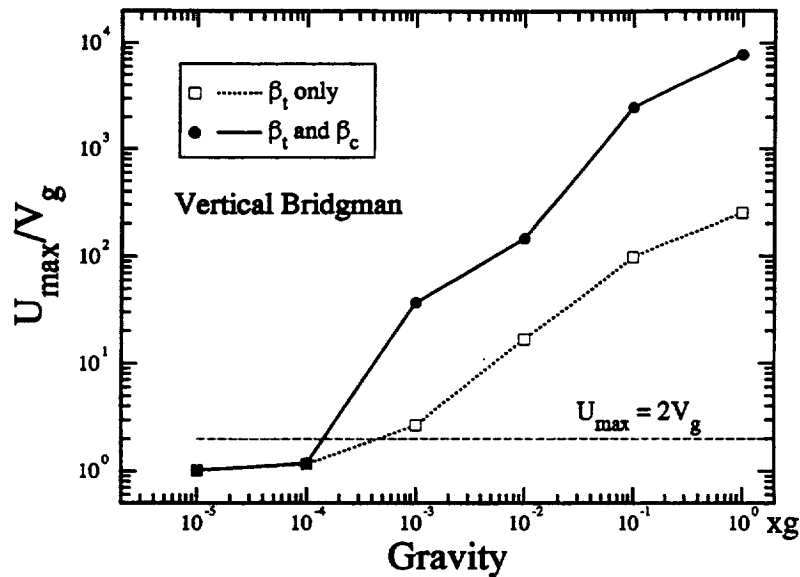


Figure 11. Effects of gravity on the strength of convection in the melt measured by the maximum total velocity, U_{\max} , which includes the growth rate V_g and the buoyancy-driven convective velocity.

rejected at the interface is first swept in a negative radial direction towards the center of the ampoule and then is carried away from the interface along the axial direction at the center. However, the rejected solute is only carried a very short distance (about twice the radius) along the axial direction and cannot go further due to the small size of the flow cell driven by the local radial thermal gradient. When the convective flow becomes stronger at high gravity levels, the radial segregation continues to increase but the axial segregation is still limited within the short range near the interface. Since the rejected solute is only circulated in the lower flow cell and cannot be passed to the larger upper flow cell, the axial mixing is incomplete. This suggests that for this particular vertical growth condition the thermal gradient contributes merely to the low level of mixing near the interface.

6.2 Effects of Solute Volumetric Expansion

For non-dilute alloy system, the density variation caused by solute volumetric expansion becomes important. For PbSnTe, scaling analysis shows that the magnitude of $\beta_t \Delta T$ and $\beta_c \Delta C$ are globally of the same order. Consequently, the solute buoyancy force is of equal importance as the thermal counterpart. In our modeling, the second set of solutions considers both the thermal and solute volumetric expansions. The results are presented in Figs. 11-13.

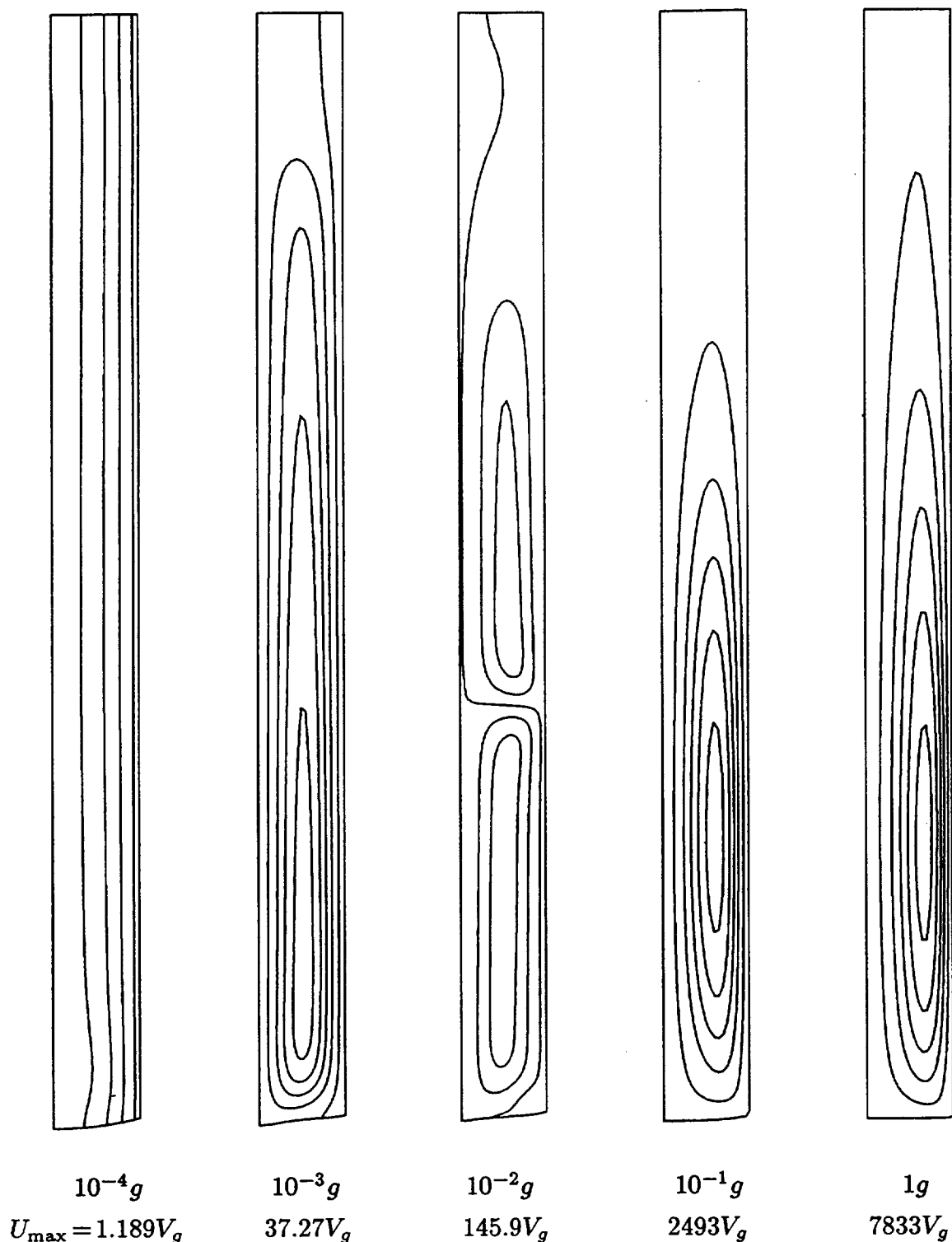


Figure 12a Contours of stream functions for the vertical growth when both the thermal and solutal buoyancy forces are considered. The flow direction of all the flow cells, except the top flow cell at $10^{-2}g$, is clockwise, i.e. the fluid flow upwards along the axis and downwards along the wall. Here the calculation of stream function is based on the total velocity and $V_g = 2.778 \mu\text{m}/\text{sec}$.

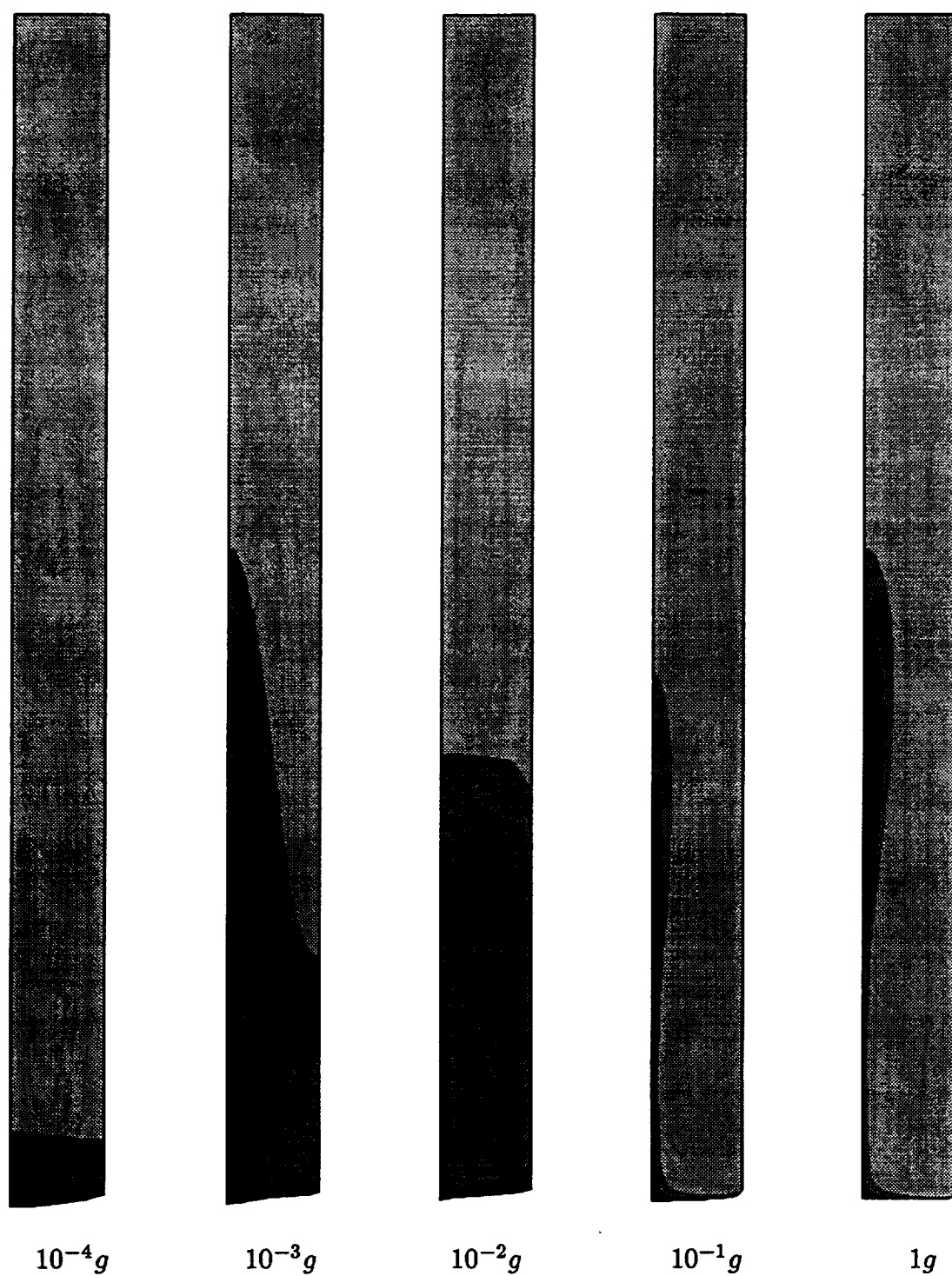


Figure 12b Simulated solute segregation in the melt corresponding to the flow fields shown in Fig. 12a. The darker grey scale represents higher solute concentration.

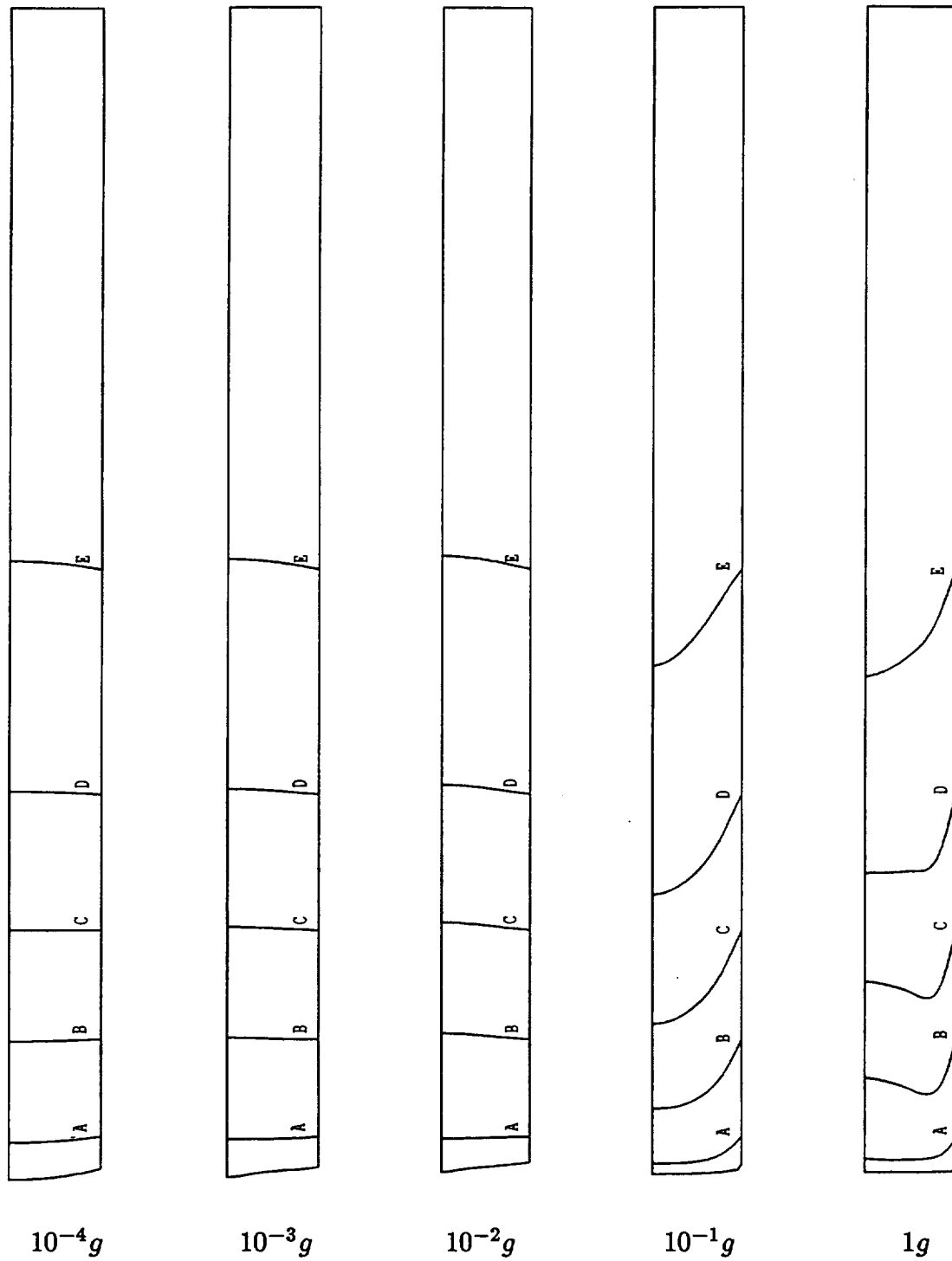


Figure 12c The effect of convective flow on the thermal field in the melt for the vertical growth when both the thermal and solutal buoyancy forces are considered. The values of the isotherm contours are: $A = 912.0$, $B = 958.9$, $C = 1005.8$, $D = 1052.7$ and $E = 1099.7^{\circ}\text{C}$.

The most obvious impact by considering the solute buoyancy force is the changes in the convective flow pattern and the significant increase in convective strength. Comparison between Fig. 10a and 12a shows that when the solutal expansion effect is included the flow field and solute segregation become quite different starting from the gravity level of $10^{-3}g$. In this case the flow pattern in the melt is greatly changed by the interaction between ∇T and ∇C . The axial thermal gradient causes material to rise in the center and flow down along the wall. This thermal buoyancy induced flow cell (the lower flow cells shown in Fig. 10a) is strengthened by the axial concentration gradient which forces the rejected lighter solute to be carried away from the interface along the centerline. As a result a single large cell is formed at $10^{-3}g$. However, the interaction between thermal and solute gradient is quite complicated. At $10^{-2}g$ two equal-size flow cells are formed as shown in Fig. 12a. The upper flow cell is then diminished again at higher gravity levels. When the solute volumetric expansion is included, the strength of the convective flow (measured by U_{\max}) is about one order of magnitude higher than that caused by thermal expansion only (for gravity levels greater than g_c as shown in Fig. 11). The results presented here demonstrate the significance of the effect of solute volumetric expansion and the interaction between the solutal and thermal fields for non-dilute alloys.

It is interesting to observe how the convective flow field changes with increase of gravity levels. At low gravity level, such as $10^{-3}g$, the flow cell shown in Fig. 12a indicates that the flow at the lower part of the ampoule can be divided vertically into two opposite flow regions, with the division line lies approximately at the middle of the radius, i.e. $r = 0.5R$. The central part $r < 0.5R$ is a cylinder with an upward flow, while the outer annular region $0.5R < r < R$ has a downward flow. Since the cross-section areas of these two regions are unequal, the average flow speed on them is different. In order to satisfy the continuity condition, the flow is faster in the smaller central region than that in the larger outer annular region. However, with increase of convection strength, the flow cell is pushed towards to the wall. As we can see from Fig. 12a, the outer annular region becomes smaller and the division line at $1g$ is much closer to the wall. This results in a thin boundary layer and a faster flow near the wall at high gravity levels. The thermal contour plots in Fig. 12c also indicate a thin thermal boundary layer at $1g$ level. These thin boundary layers render great difficulties for numerical solution, causing slow-down in convergence or even divergence of the nonlinear iterations. These difficulties occurred in our computation were also reported in the literature [19].

The effect of solute gradient on segregation is also significant. On the interface, the radial solute gradient acts in an opposite direction to the thermal radial gradient and tends to reduce the radial segregation. At the center of the sample, however, the axial solute gradient acts in the same direction as the axial thermal gradient and tends to enhance the axial segregation. This results in a weaker local radial segregation near the interface and a much more complete mixing at high gravity levels, as can be seen in Fig. 12b and 13.

In order to describe quantitatively the transition from diffusion-controlled growth (without bulk convection) to growth with intensive laminar convective mixing, we compute two conventional segregation parameters. The first is the *effective segregation coefficient* k_{eff} defined as [19]

$$k_{\text{eff}} \equiv k \langle C \rangle_I / \langle\langle C \rangle\rangle \quad (6.1)$$

where $\langle C \rangle_I$ is the lateral average of solute concentration over the solid/liquid interface and $\langle\langle C \rangle\rangle$ is the volumetric average of solute concentration in the melt. The second is the percentage radial segregation ΔC defined as

$$\Delta C \equiv |\delta C|_{\text{max}} / C_0 \quad (6.2)$$

or

$$\Delta C \equiv |C_{\text{top}} - C_{\text{bottom}}| / C_0 . \quad (6.3)$$

Here $|\delta C|_{\text{max}}$ is the maximum difference in concentration at the interface. For directional solidification, diffusion-controlled growth with a planar interface leads to uniform solute distribution in radial direction, thus we have $\Delta C = 0$. If the melt is sufficiently long that the diffusion layer near the interface occupies only a small fraction of the total length, k_{eff} approaches unity when there is no convective flow in the melt other than the unidirectional growth velocity V_g . The other limit of k_{eff} represents the steady state well-mixed growth in which the intense convection leads to a complete mixing in the melt. In this case the value of k_{eff} approaches k .

The computed segregation coefficients for the vertical growth are plotted as a function of gravity levels in Fig. 13. Here the quantitative axial and radial segregation analysis is consistent with the results seen in Fig. 10b and 12b. For thermal buoyancy induced flow case, the values of k_{eff} are very close to one at all gravity levels, which indicates the diffusion-dominated growth in axial segregation even though the local radial segregation may be quite large at high gravity levels as suggested by the values of ΔC .

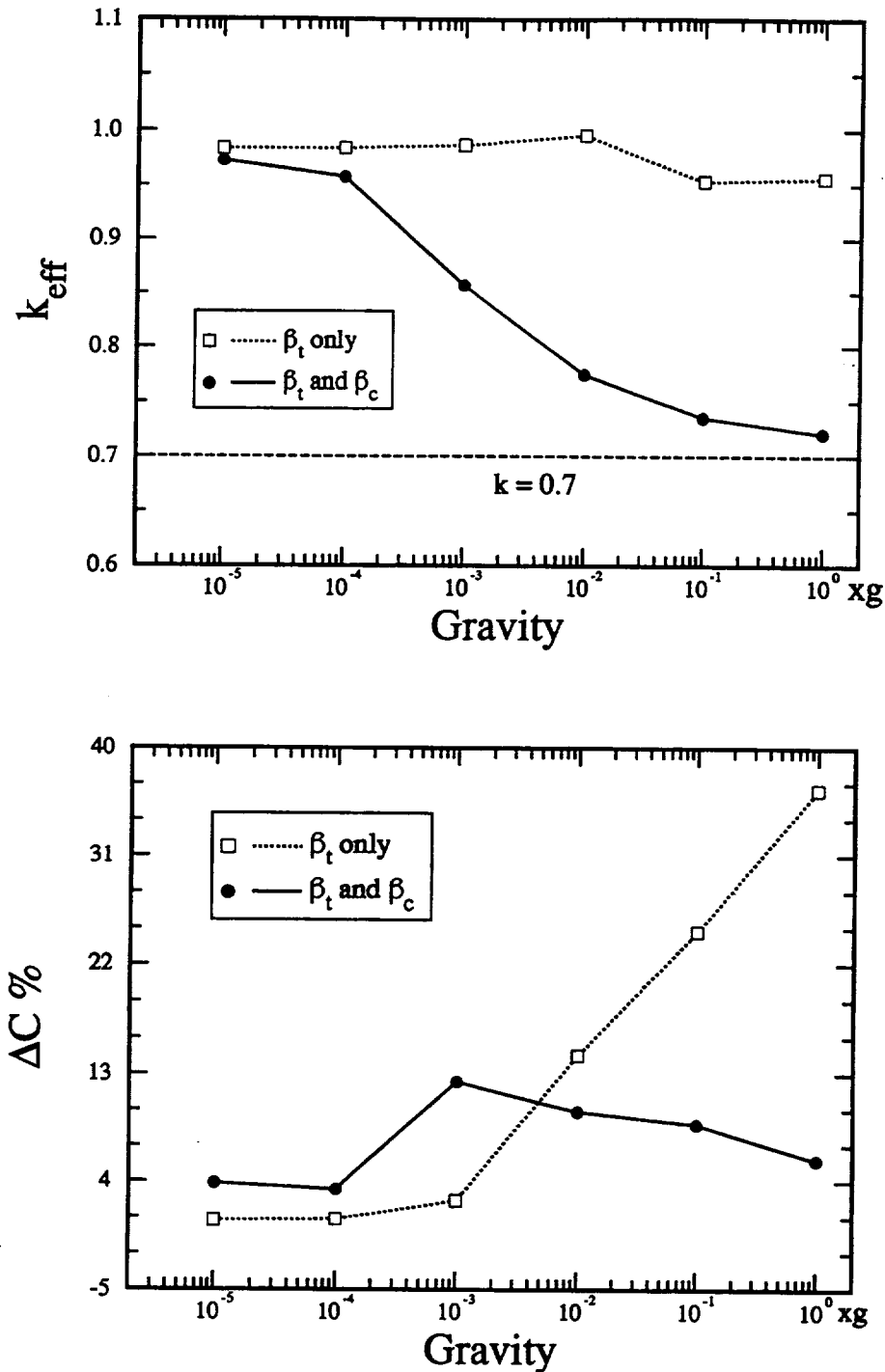


Figure 13. A quantitative description of the effects of gravity on the axial solute segregation (a) measured in terms of the effective segregation coefficient, k_{eff} and the radial solute segregation (b). The results are based on the axisymmetric model for the vertical growth and the values of ΔC were calculated from the liquid side of the interface. The results labeled by β_t considers thermal buoyancy force only.

When both thermal and solute buoyancy forces are considered, the calculated k_{eff} values in Fig. 13(a) show a diffusion-controlled growth at low gravity levels. k_{eff} is very close to k at high gravity levels which indicates that a well-mixed state has been achieved. Radial segregation results show that weak convection (in the range $10^{-6}g$ to $10^{-4}g$) and strong convection (at $1g$) both produce low radial segregation, while the intermediate gravity levels produce high radial segregation. As shown in Fig. 13(b), ΔC has a local maximum at $10^{-3}g$, which is very close to the gravity level predicted by the critical g_c shown in Fig. 11. The plots of k_{eff} and ΔC v.s. the magnitude of gravity presented here agree well with the schematic curves given by Kim, Adornato and Brown in [19].

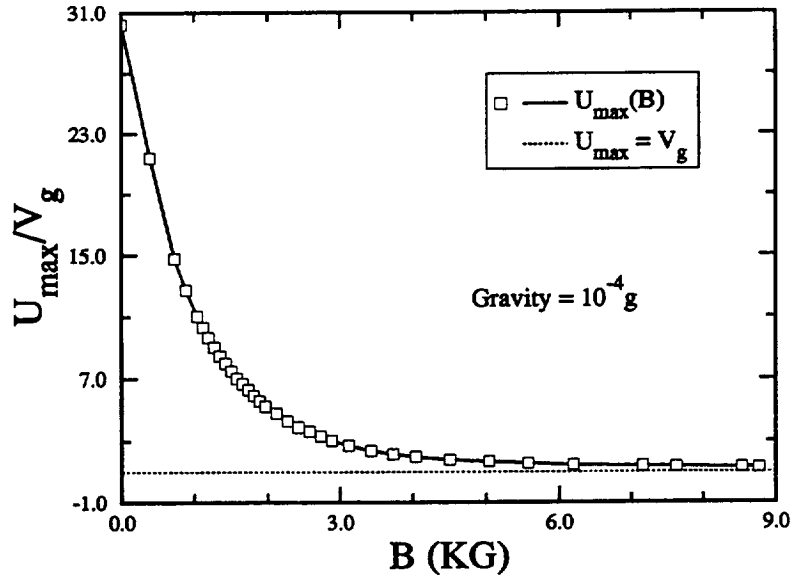


Figure 14. Effects of an axially imposed magnetic field on the strength of convective flow in the melt measured by the maximum total velocity, U_{max} . The results are based on the vertical growth model with $R = 1\text{cm}$, $V_g = 0.5\mu\text{m/sec}$ and $\beta_c = 0$.

6.3 Magnetic Damping

The action of an axial magnetic field on convection in the melt is to interfere with the radial velocity component. As pointed out in ref. [19], at large B the magnitude of the radial velocity decreases proportionally to the square of the strength of magnetic induction. The axial velocity component is not affected by the magnetic field except in the coupling through the incompressibility condition. When the magnetic field is strong enough, an almost uniaxial flow (i.e. $u_z = V_g$, $u_r = 0$) can always be obtained. One of the

goals of this study is to quantitatively determine the required magnetic field levels at which the diffusion-controlled growth can be achieved in orbit. In Fig. 14 and 15 we provide a typical analysis of the effects of magnetic damping for vertical Bridgman at a low gravity of $10^{-4}g$. Note that the results presented in this subsection are based on a larger ampoule radius $R = 1cm$ and a slower growth rate $V_g = 0.5\mu m/sec$. With these conditions, $10^{-5}g$ resulted in an almost diffusive growth without magnetic field.

Our numerical results suggest that magnetic damping on the convective flow in the melt is practically effective for micro-gravity crystal growth. By considering the magnetic damping as a continuous loading process with the increase of B , the typical U_{max} v.s. B curve given in Fig. 14 shows that there are mainly two stages during the magnetic damping process. The first is a rapid change stage in which the strength of the convective flow in the melt is significantly reduced with an increase of magnetic field strength. The second is a slow (asymptotic) change stage during which the velocity decreases very slowly with an increase of B . These two stages can be clearly seen in Fig. 14. In this case, over 90% of the original strength of convection is damped when B is increased from zero to 3000 Gauss. However it requires another 6000 Gauss to eliminate nearly all of the original velocity strength.

In Fig. 15 we plot the interface shape, radial and axial solute segregation at several B levels. Fig. 15(b) shows how magnetic damping affects the radial segregation on the interface. Here the change of radial segregation with the increase of B is not monotonic, it is reduced to a local minimum at about $B = 1.5KG$ and then increased again. Fig. 15(c) and (d) shows the effectiveness of magnetic damping on the axial segregation under the microgravity condition. At $B \approx 3KG$ the axial segregation is very close to a diffusion-dominated growth state.

At high gravity levels, our results suggest that the axially imposed magnetic field is not effective for suppressing convective flow in the melt. Fig. 16 shows an example of magnetic damping for the vertical growth on earth. As we can see that the u_{max} is still about 1000 times higher than V_g at $B = 25KG$ and the decrease of u_{max} is much slower than that at the gravity level of $10^{-2}g$. The scaling analysis suggests that the required magnetic field strength for the terrestrial growth will be much higher than the generally available 50KG in order to achieve the diffusion-dominated growth condition.

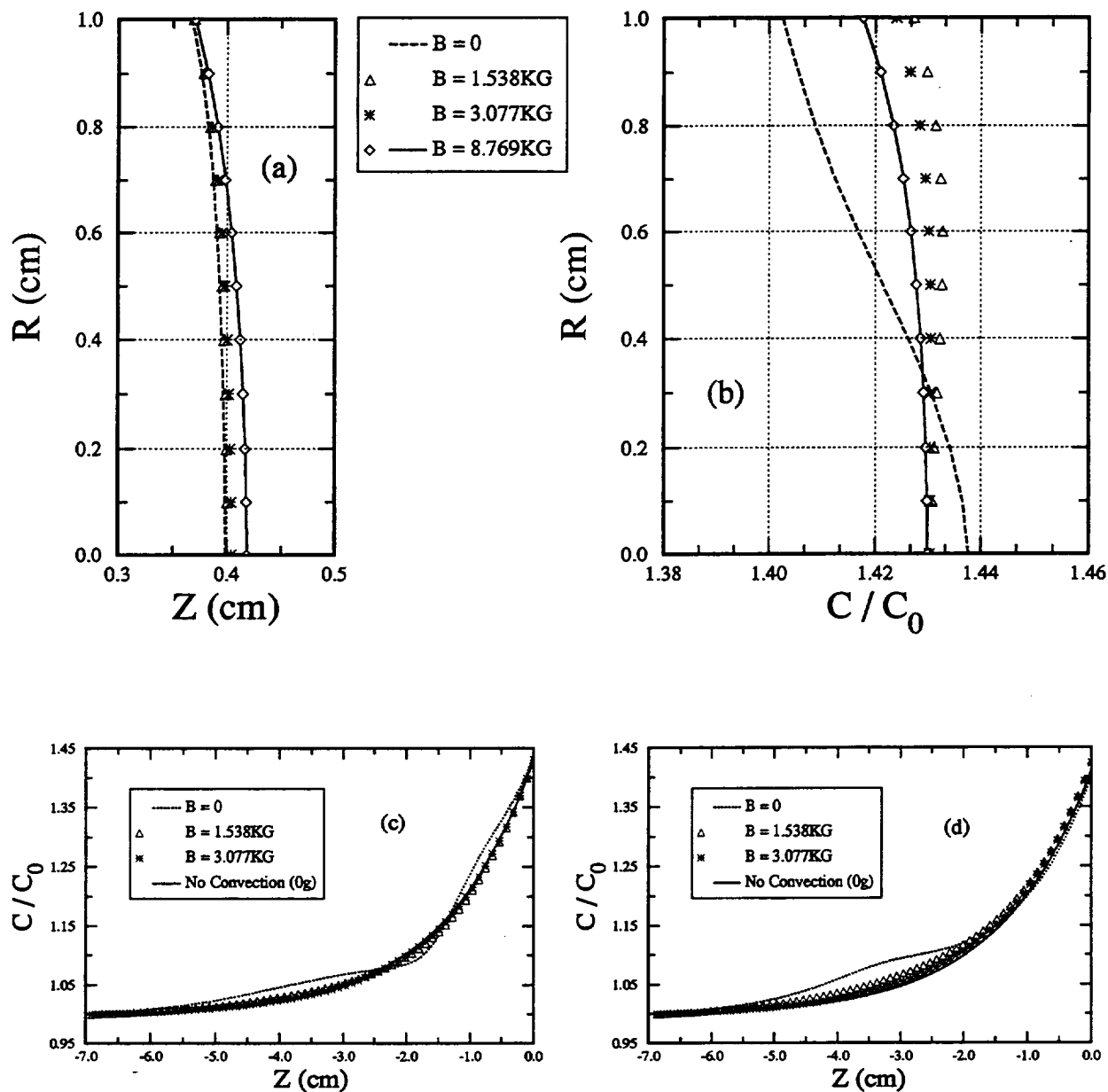


Figure 15. Numerical solutions of the vertical Bridgman growth with increasing magnetic field strength measured in kilo-Gauss. (a) Liquid/solid interface shapes; (b) Radial solute segregation at interface; (c) Axial segregation at the center of ampoule ($R = 0$); (d) Axial segregation on the surface of sample ($R = 1.0 \text{ cm}$).

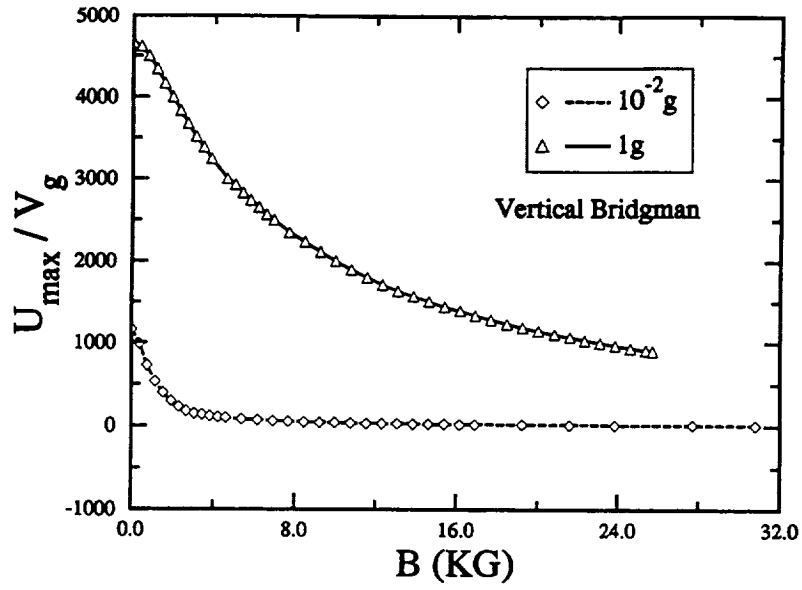


Figure 16. Magnetic damping for the high gravity level of $1g$. The results are based on the vertical growth model with $R = 1cm$, $V_g = 0.5\mu m/sec$ and $\beta_c = 0$.

7. HORIZONTAL BRIDGMAN GROWTH

Vertical Bridgman represents an idealized configuration which may only exist on earth. In space, the situation is quite different. First, it is practically impossible to exactly align the furnace axis with the residual gravitational vector. Second, any deviation of the furnace axis from gravity direction will dramatically change the flow field. The results presented in Fig. 17(a) and (b) suggest that even a 1° mis-alignment at low gravity of $10^{-4}g$ can completely distort the axisymmetric flow pattern and increase the strength of convection by a factor of up to seven in our particular case.

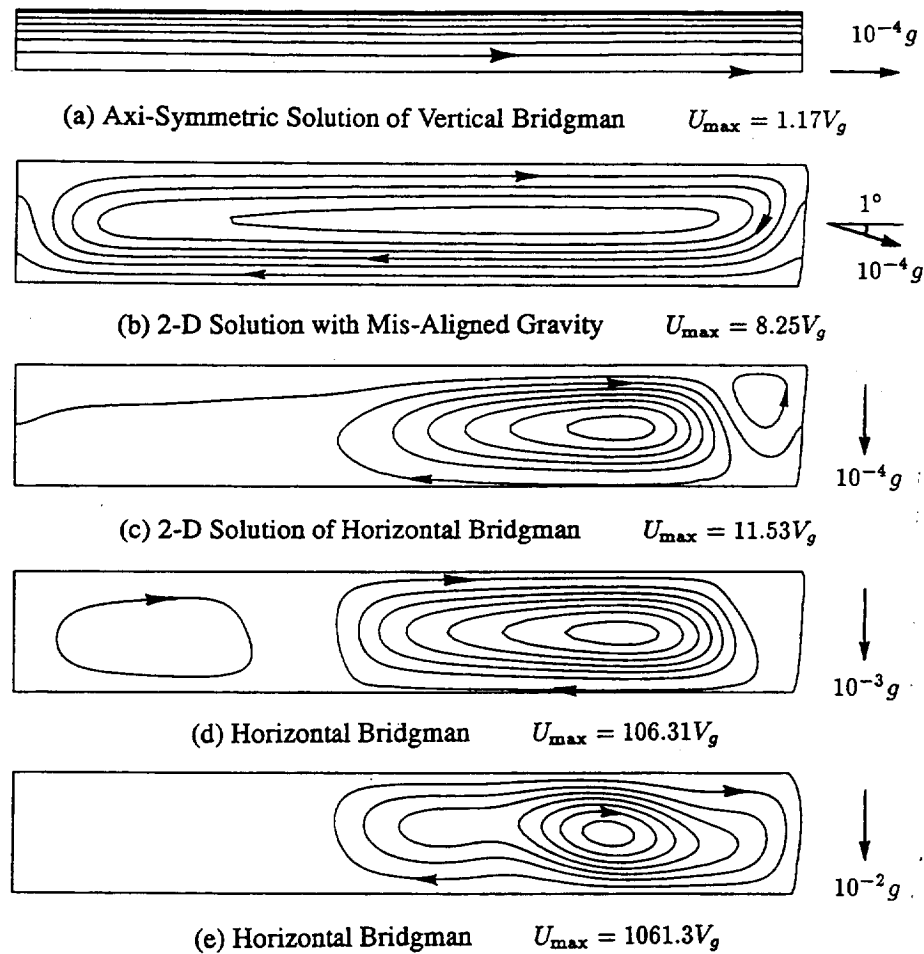


Figure 17. Effects of orientation and magnitude of gravity vector on the fluid motion in the melt of PbSnTe.

To study the effects of the orientation and magnitude of gravity, we present in Fig. 17(c)-(d) the flow fields in the melt, and in Fig. 18 the interface shape, radial and axial segregation for horizontal Bridgman growth at four typical gravity levels. Note That

the solutions presented in this section consider the density variation caused by both the thermal and solute volumetric expansions.

For horizontal Bridgman, the growth at $10^{-5}g$ is very close to diffusion-dominated state as indicated in the axial segregation plots in Fig. 18(c) and (d). At $10^{-4}g$ the thermal buoyancy induced flow cell in the center part rotates in the same direction as in the vertical Bridgman configuration. However, the radial solute segregation and ∇C_r are locally strong enough to force the rejected solute flow up along the interface and form a clockwise flow cell near the interface. For a given growth speed V_g , this solutal buoyancy induced flow cell exists only at low g when the mixing is incomplete and becomes less pronounced as gravity increases. When gravity $\geq 10^{-2}g$ the small flow cell near the interface vanishes and the thermal convection grows to a larger cell. This strong convection results in a complete mixing and a much more uniform solute distribution along both the axial and radial directions, as can be seen in Fig. 18(b)-(d).

For the horizontal growth, the axial magnetic field is less efficient than for the vertical growth. A typical magnetic damping analysis is presented in Fig. 19. As we can see from Fig. 19(d), a three Kilo-Gauss field can bring down about 90% of the convection strength at $10^{-4}g$. However, a much higher magnetic field (about 40KG) is required to reach to the diffusion-dominated growth state.

8. CONCLUSIONS

Since the alignment of furnace axis with residual gravitational acceleration aboard any orbiter cannot be practically guaranteed to within a small fraction of a degree, we should only resort to examining the results obtained from the horizontal Bridgman growth models. Even though the DC acceleration levels typical on the shuttle are $< 10^{-5}g$ (depending on the furnace location relative to C.G.), we recommend using a worst case scenario in which the g -vector is perpendicular to the ampoule axis. Furthermore, it has been known that isolated large amplitude peaks in the order of $O(10^{-3})g$ are common in space. Therefore, a conservative estimate at this time can probably be obtained by using the horizontal Bridgman model with $10^{-4}g$ DC case. Our results show that a magnetic field of few kilo-Gauss will be sufficient to substantially reduce the effects of buoyancy-induced convection on the solute segregation. Investigation of a $10^{-5}g$ DC case with a time-dependent $10^{-3}g$ acceleration pulse will be pursued later.

Future plans call for ground work in a magnetic furnace and continued modeling work on predicting and comparing with experimental data for a systematic examination

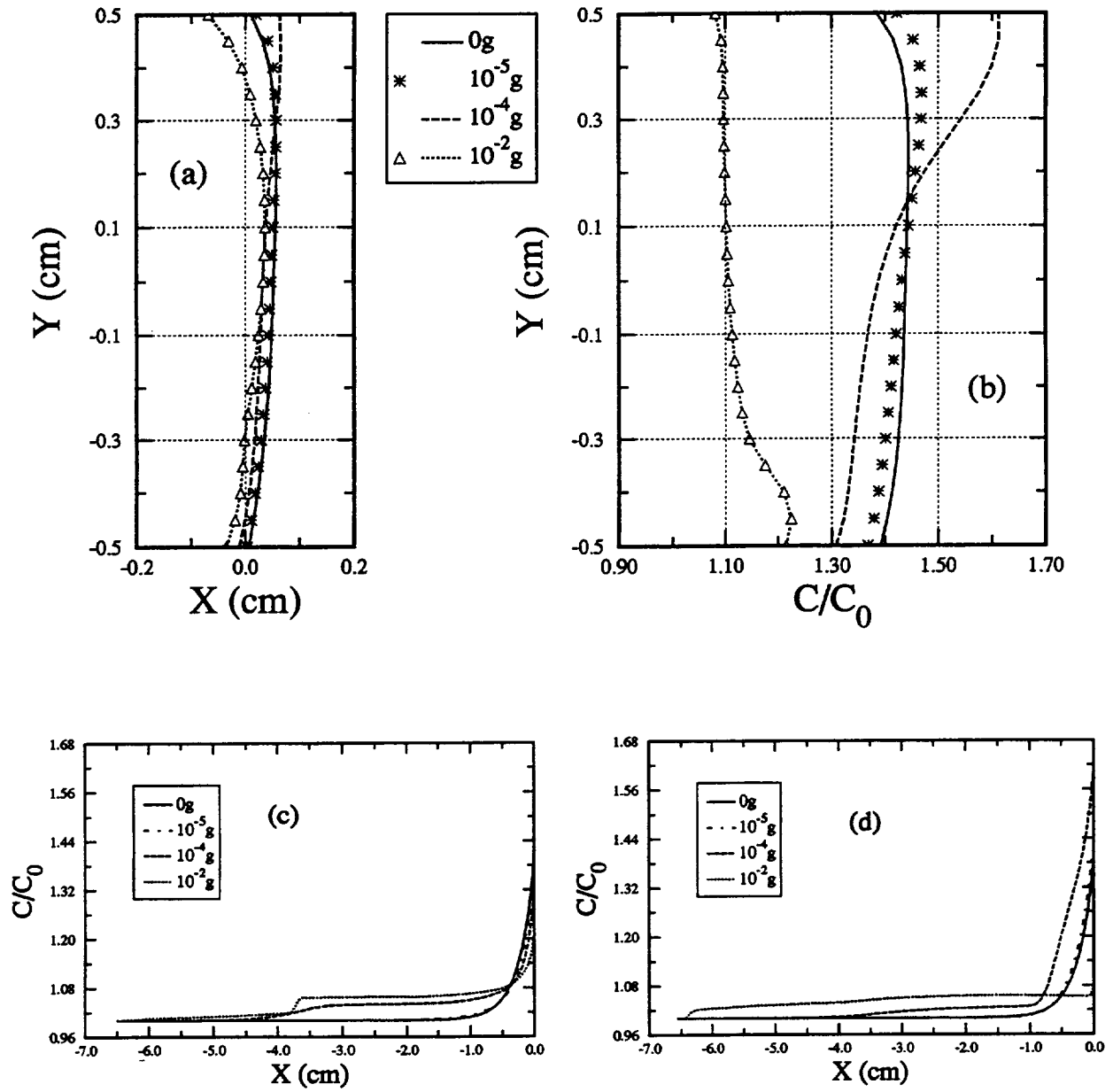


Figure 18. Modeled horizontal Bridgman growth at $V_g = 1 \text{ cm/hour}$ and three low gravity levels. (a) Liquid/solid interface shapes; (b) Radial solute segregation at interface; (c) Axial segregation on bottom boundary ($y = -0.5 \text{ cm}$); (d) Axial segregation on top ($y = 0.5 \text{ cm}$).

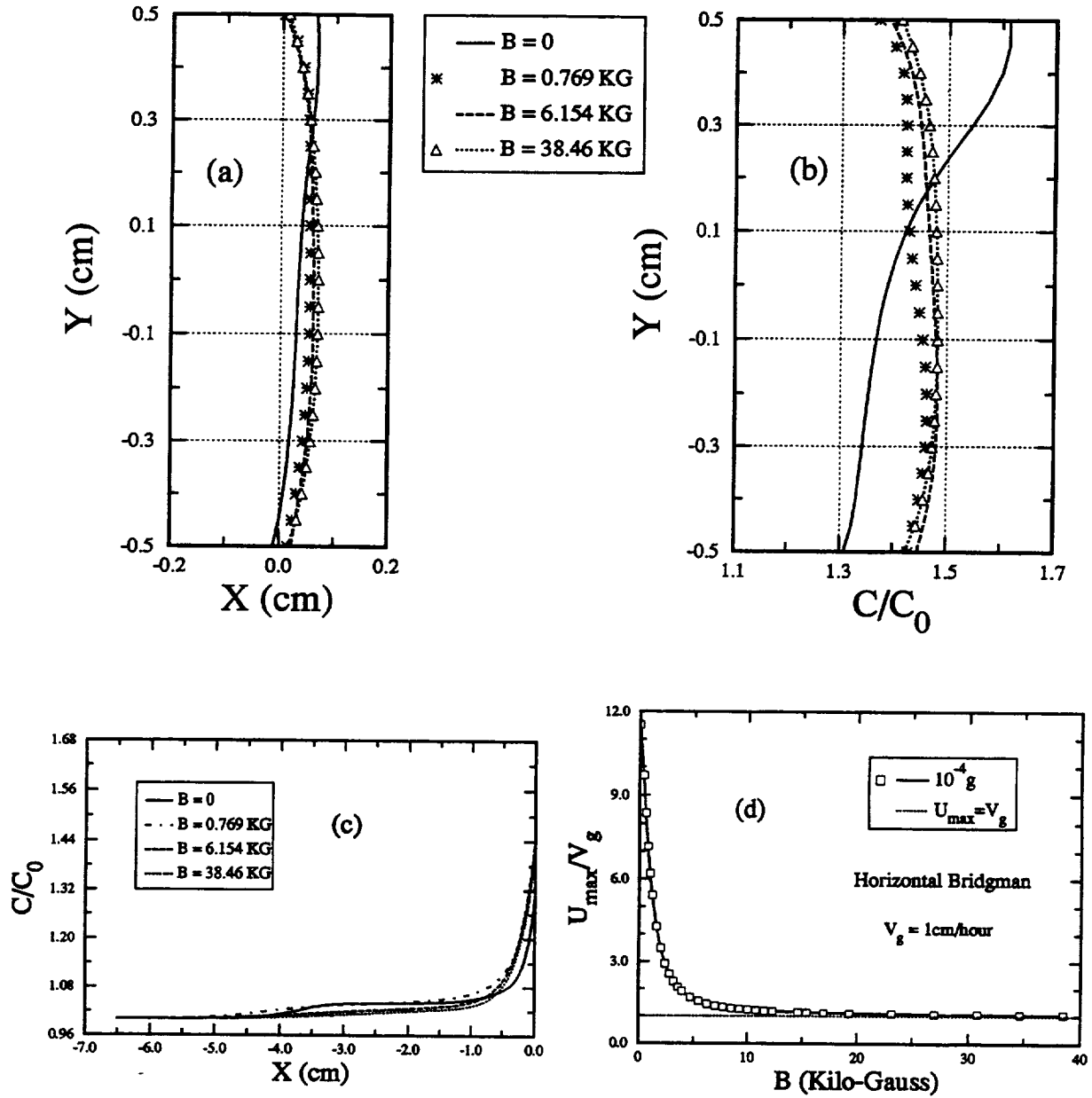


Figure 19. Numerical solutions of the horizontal Bridgman growth with increasing magnetic field strength measured in kilo-Gauss. (a) Liquid/solid interface shapes; (b) Radial solute segregation at interface; (c) Axial segregation on bottom boundary ($y = -0.5$ cm); (d) Damping of U_{\max} with increase of B .

of the phenomena at hand, and for specifying the required magnetic field for microgravity experiments.

ACKNOWLEDGMENTS

This work was supported by NASA's Micro-gravity Science and Application Program (Grant # NAG 3-1096 and NCC 3-208). We also would like to thank Natarajan Ramanan and Stephan Fatschel at Fluid Dynamics International for their technical support and for Dr. Ramanan's very helpful comments on using the free surface solution approach in FIDAP.

REFERENCES

- [1] M.C. Flemings, *Solidification Processing*, McGraw-Hill, (1974).
- [2] M.A. Brown, Theory of Transport Processes in Single Crystal Growth from the Melt, *AIChE J*, Vol. 34 (1988), pp. 881-911.
- [3] M. Yao and H.C. de Groh III, Three-Dimensional Finite Element Method Simulation of Bridgman Crystal Growth and Comparison with Experiments, *Num. Heat Transf., Part A*, Vol. 24 (1993), pp. 393-412.
- [4] M. Yao, R. Raman and H.C. de Groh III, Numerical Modeling of Bridgman Growth in Space with MEPHISTO, *Proceedings of Int. Conf. Computational Eng. Science*, 7/30-8/3, 1995, Mauna Lani, Big Island Hawaii (to appear).
- [5] P.M. Adornato and R.A. Brown, Convection and Segregation in Directional Solidification of Dilute and Non-Dilute Binary Alloys: Effects of Ampoule and Furnace Design, *J. Crystal Growth*, Vol. 80 (1987) pp. 155-190.
- [6] D.J. Knuteson, A.L. Fripp, G.A. Woodell, W.J. Debnam and R. Narayanan, Oscillation Phase Relations in a Bridgman System, *J. Crystal Growth*, Vol. 109 (1991) p. 127.
- [7] D.J. Knuteson, A.L. Fripp, G.A. Woodell, W.J. Debnam and R. Narayanan, Unsteady Convection in Tin in a Bridgman Configuration, *J. Crystal Growth*, Vol. 110 (1991) p. 348.
- [8] W.A. Arnold, D.A. Jacqmin, R.L. Gaug and A. Chait, Three-Dimensional Flow Transport Modes in Directional Solidification during Space Processing, *J. Spacecraft and Rockets*, Vol. 28 (1991) pp. 238-234.
- [9] D.T.J. Hurle, *Crystal Pulling from the Melt*, Springer-Verlag, (1993).

- [10] H.P. Utech and M.C. Flemings, Elimination of Solute Banding in Indium Antimonide Crystals By Growth in a Magnetic Field, *J. Appl. Phys.*, Vol. 37 (1966) pp. 2021-2024.
- [11] H.P. Utech and M.C. Flemings, Thermal Convection in Metal Crystal Growth: Effect of a Magnetic Field, *Crystal Growth*, ed. H.S. Peiser, Pergamon Press, Oxford, 1967.
- [12] H.A. Chedzey and D.T.J. Hurle, *Nature*, Vol. 210 (1966) p. 933.
- [13] T. Suzuki, N. Isawa, Y. Okubo and K. Hoshi, *Proc. 4th Int. Symp. on Silicon*, Materials Science & Technology: Semiconductor Silicon 1981 (EPS Pennington, NJ 1981).
- [14] R.W. Series and D.T.J. Hurle, The Use of Magnetic Fields in Semiconductor Crystal Growth, *J. Crystal Growth*, Vol. 113 (1991) pp. 305-328.
- [15] K. Hoshikawa, H. Kohda, H. Hirata and H. Nakanishi, *Japan. J. Appl. Phys.*, Vol. 19 (1980) L33.
- [16] K. Hoshikawa, *Japan. J. Appl. Phys.*, Vol. 21 (1982) L545.
- [17] R.W. Series, Effect of a Shaped Magnetic Field on Czochralski Silicon Growth, *J. Crystal Growth*, Vol. 97 (1989) p. 92.
- [18] H. Hirata and K. Hoshikawa, Silicon Crystal Growth in a Magnetic Field, *J. Crystal Growth*, Vol. 96 (1989) p. 747.
- [19] D.H. Kim, P.M. Adornato and R. Brown, Effect of Vertical Magnetic Field on Convection and Segregation in Vertical Bridgman Crystal Growth, *J. Crystal Growth*, Vol. 89 (1988) pp. 339-356.
- [20] K.M. Kim, Suppression of Thermal Convection by Transverse Magnetic Field, *J. Electrochem. Soc.*, Vol. 129 (1982) p. 427.
- [21] S. Sen, R.A. Lefever and W.R. Wilcox, Influence of Magnetic Field on Vertical Bridgman-Stockbarger Growth of InGaSb, *J. Crystal Growth*, Vol. 43 (1978) p. 526.
- [22] D.H. Matthiesen, M.J. Wargo, S. Motakef, D.J. Carlson, J.S. Nakos and A.F. Witt, Dopant Segregation during Vertical Bridgman-Stockbarger Growth with Stabilization by Strong Magnetic Fields, *J. Crystal Growth*, Vol. 85 (1987) p. 557.
- [23] C.H. Su, S.I. Lehoczky and F.R. Szofran, Directional Solidification of HgCdTe and HgZnTe in a Transverse Magnetic Field, *J. Crystal Growth*, Vol. 109 (1991) p. 392.
- [24] S. Motakef, Magnetic Field Elimination of Convective Interference with Segregation during Vertical Bridgman Growth of Doped Semiconductors, *J. Crystal Growth*, Vol. 89 (1988) p. 339.
- [25] P.J. Prescott and F.P. Incropera, Magnetically Damped Convection During Solidification of a Binary Metal Alloy, *J. Heat Transfer*, Vol. 115 (1993) pp. 302-310.

- [26] W.D. Bennon and F.P. Incropera, A Continuum Model for Momentum, Heat and Species Transport in Binary Solid-Liquid Phase Change Systems - I. Model Formulation, *Int. J. Heat Mass Transfer*, Vol. 30 (1987) pp. 2161-2170.
- [27] P.J. Prescott and F.P. Incropera, The Effect of Turbulence on Solidification of a Binary Metal Alloy with Electromagnetic Stirring, HTD-Vol. 280 ASME (1994) pp. 59-69.
- [28] M. Engleman, *FIDAP Theoretical Manual (version 7)*, Fluid Dynamics International, Inc., 500 Davis St. Suite 600, Evanston, IL 60201, 1993.
- [29] R.K. Crouch, A.L. Fripp, W.J. Debnam, I.O. Clark and F.M. Carlson, Ground Based Studies for the Space Processing of Lead-Tin-Telluride, in *Materials Processing in the Reduced Gravity Environment of Space*, ed. G.E. Rindone, Elsevier (1982) pp. 611-617.
- [30] A.L. Fripp, F.R. Szofran and A. Chait, Melt Stabilization of PbSnTe in a Magnetic Field, NRA Proposal NRA-91-OSSA-20 (1991).
- [31] S.R. Coriell, M.R. Cordes, W.J. Boettinger and R.F. Sekerka, Convective and Interfacial Instabilities During Unidirectional Solidification of a Binary Alloy, *J. Crystal Growth*, Vol. 49 (1980) p. 13.
- [32] A.L. Fripp, R.K. Crouch, W.J. Debnam, G.A. Woodell, I.O. Clark, F.M. Carlson and R.T. Simchick, Growth of Compound Semiconductor Alloys, in *Microgravity Science and Applications Flight Programs - Selected Papers*, NASA Tech. Memorandum #4069, October 1988.
- [33] R.E. Taylor and H. Groot, Thermophysical Properties of PbSnTe: A Report to NASA (Langley), *TPRL 203*, Thermophysical Properties Research Lab, School of Mechanical Engineering, Purdue University, West Lafayette, Indiana, Jan. 1980.
- [34] R.E. Taylor and H. Groot, Thermophysical Properties of PbSnTe (Part II): A Report to NASA, *TPRL 255*, July 1981.
- [35] R.E. Taylor and H. Groot, Thermophysical Properties of PbSnTe (Part III): A Report to NASA, *TPRL 255A*, Sept. 1982.
- [36] R.E. Taylor and H. Groot, Thermophysical Properties of PbSnTe: A Report to NASA, *TPRL 320*, March 1983.
- [37] J.S. Harris, J.T. Longo, E.R. Gertner and J.E. Clarke, The PbSnTe Phase Diagram and Its Application to The Liquid Phase Epitaxial Growth of $Pb_{1-x}Sn_xTe$, *J. Crystal Growth*, Vol. 28 (1975) pp. 334-342.
- [38] V.M. Glazov, S.N. Chizhevskaya and N.N. Glagoleva, *Liquid Semiconductors*, Plenum Press, NY 1969.

- [39] A.L. Fripp, Description of Experiment Specimens, notes, 1992.
- [40] T.J. Jasinski, W.M. Rohsenow and A.F. Witt, *J. Crystal Growth*, Vol. 61 (1983) p. 339.
- [41] C.J. Chang and R.A. Brown, Radial Segregation Induced by Natural Convection and Melt/solid Interface Shape in Vertical Bridgman Growth, *J. Crystal Growth*, Vol. 63 (1983) pp. 343-364.
- [42] J. Crank, *Free and Moving Boundary Problems*, Clarendon Press, Oxford, 1984.
- [43] H. Saito and L.E. Scriven, Study of Coating Flow by the Finite Element Method, *J. Comp. Phys.*, Vol. 42 (1981) p. 53.
- [44] L.I. Rubinstein, *The Stefan Problem*, Translations of Mathematical Monographs, Vol. 27, American Mathematical Society, Providence, RI 02904 (1971) p. 52.
- [45] R.D. Cook, D.S. Malkus and M.E. Plesha, *Concepts and Applications of Finite Element Analysis*, 3rd ed., John Wiley & Sons, New York, 1989.
- [46] L.N. Hjellming and J.S. Walker, Melt Motion in A Czochralski Crystal Puller with An Aixal Magnetic Field: Isothermal Motion, *J. Fluid Mech.*, Vol. 164 (1986) pp. 237-273.
- [47] L.N. Hjellming and J.S. Walker, Melt Motion in A Czochralski Crystal Puller with An Aixal Magnetic Field: Motion due to Buoyancy and Thermalcapillarity, *J. Fluid Mech.*, Vol. 182 (1987) pp. 335-368.
- [48] L.N. Hjellming and J.S. Walker, Mass Transport in A Czochralski Crystal Puller with An Aixal Magnetic Field: Melt Motion due to Crystal Growth and Buoyancy, *J. Crystal Growth*, Vol. 92 (1988) pp. 371-389.
- [49] L.N. Hjellming, A Thermal Model for Czochralski Silicon Crystal Growth with An Aixal Magnetic Field, *J. Crystal Growth*, Vol. 104 (1990) pp. 327-344.

REPORT DOCUMENTATION PAGE			Form Approved OMB No. 0704-0188	
Public reporting burden for this collection of information is estimated to average 1 hour per response, including the time for reviewing instructions, searching existing data sources, gathering and maintaining the data needed, and completing and reviewing the collection of information. Send comments regarding this burden estimate or any other aspect of this collection of information, including suggestions for reducing this burden, to Washington Headquarters Services, Directorate for Information Operations and Reports, 1215 Jefferson Davis Highway, Suite 1204, Arlington, VA 22202-4302, and to the Office of Management and Budget, Paperwork Reduction Project (0704-0188), Washington, DC 20503.				
1. AGENCY USE ONLY (Leave blank)		2. REPORT DATE July 1995		3. REPORT TYPE AND DATES COVERED Technical Memorandum
4. TITLE AND SUBTITLE Numerical Modeling of Bridgman Growth of PbSnTe in a Magnetic Field			5. FUNDING NUMBERS WU-963-35-0B	
6. AUTHOR(S) Minwu Yao, Arnon Chait, Archibald L. Fripp, and William J. Debnam				
7. PERFORMING ORGANIZATION NAME(S) AND ADDRESS(ES) National Aeronautics and Space Administration Lewis Research Center Cleveland, Ohio 44135-3191			8. PERFORMING ORGANIZATION REPORT NUMBER E-9773	
9. SPONSORING/MONITORING AGENCY NAME(S) AND ADDRESS(ES) National Aeronautics and Space Administration Washington, D.C. 20546-0001			10. SPONSORING/MONITORING AGENCY REPORT NUMBER NASA TM-106996	
11. SUPPLEMENTARY NOTES Prepared for the Sixth FIDAP Users Conference sponsored by Fluid Dynamics International, Chicago, Illinois, April 30—May 2, 1995. Minwu Yao, Ohio Aerospace Institute, 22800 Cedar Point Road, Cleveland, Ohio, (work funded by NASA Grant NAG3-1096 and NCC3-208). Arnon Chait, NASA Lewis Research Center; Archibald L. Fripp and William J. Debnam, NASA Langley Research Center. Responsible person, Arnon Chait, organization code 5110, (216) 433-3558.				
12a. DISTRIBUTION/AVAILABILITY STATEMENT Unclassified - Unlimited Subject Categories 29 and 34 This publication is available from the NASA Center for Aerospace Information, (301) 621-0390.			12b. DISTRIBUTION CODE	
13. ABSTRACT (Maximum 200 words) In this work we study heat and mass transport, fluid motion and solid/liquid phase change in the process of steady Bridgman growth of Pb_8Sn_2Te (LTT) in an axially-imposed uniform magnetic field under terrestrial and microgravity conditions. In particular, this research is concerned with the interrelationships among segregation, buoyancy-driven convection and magnetic damping in the LTT melt. The main objectives are to provide a quantitative understanding of the complex transport phenomena during solidification of the non-dilute binary of LTT, to provide estimates of the strength of magnetic field required to achieve the desired diffusion-dominated growth, and to assess the role of magnetic damping for space and earth based control of the buoyancy-induced convection. The problem was solved by using FIDAP and numerical results for both vertical and horizontal growth configurations with respect to the acceleration of gravity vector are presented.				
14. SUBJECT TERMS Crystal growth; Magnetic fields; Microgravity			15. NUMBER OF PAGES 54	
			16. PRICE CODE A04	
17. SECURITY CLASSIFICATION OF REPORT Unclassified	18. SECURITY CLASSIFICATION OF THIS PAGE Unclassified	19. SECURITY CLASSIFICATION OF ABSTRACT Unclassified	20. LIMITATION OF ABSTRACT	

